Solar Physics
DOI: 10.1007/•••••-•••-•••-••••-•

The Sunrise Chromospheric Infrared Spectro-Polarimeter SCIP: an instrument for SUNRISE III

Y. Katsukawa[1,2,3] · J. C. del Toro Iniesta[4,5] · S. K. Solanki[6] · M. Kubo[1] · H. Hara[1] · T. Shimizu[7] · T. Oba[6,8] · Y. Kawabata[1] · T. Tsuzuki[1] · F. Uraguchi[1] · K. Shinoda[1] · T. Tamura[1] · Y. Suematsu[1] · T. Matsumoto[9,1] · R. T. Ishikawa[10] · Y. Naito[2,1] · K. Ichimoto[11] · S. Nagata[11] · T. Anan[12] · D. Orozco Suárez[4,5] · E. Sanchis Kilders[13,5] · M. Balaguer Jiménez[4,5] · A.C. López Jiménez[4,5] · C. Quintero Noda[14,15] · D. Álvarez García[4,5] · J.L. Ramos Más[4,5] · J.P. Cobos Carrascosa[4,5] · P. Labrousse[4,5] · B. Aparicio del Moral[4,5] · A. Sánchez Gómez[4,5] · D. Hernández Expósito[14,5] · E. Bailón Martínez[4,5] · J.M. Morales Fernández[4,5] · A. Moreno Mantas[4,5] · A. Tobaruela[4,5] · I. Bustamante[4,5] · F.J. Bailén[4,5] · J. Blanco Rodríguez[13,5] · J.L. Gasent Blesa[13,5] · P. Rodríguez Martínez[13,5] · A. Ferreres[13,5] · D. Gilabert Palmer[13,5] · J. Piqueras Carreño[16,5] · I. Pérez Grande[16,5] · I. Torralbo[16,5] · A. Álvarez-Herrero[17,5] · A. Korpi-Lagg[6] · A. Gandorfer[6] · T. Berkefeld[18] · P. Bernasconi[19] · A. Feller[6] · T.L. Riethmüller[6] · H.N. Smitha[6] · V. Martínez Pillet[14] · B. Grauf[6] · A. Bell[18] · M. Carpenter[19]

© The author(s) ••••

Y. Katsukawa
yukio.katsukawa@nao.ac.jp

arXiv:2603.17929v3 [astro-ph.SR] 31 May 2026

Abstract The SUNRISE balloon-borne solar observatory is equipped with a one-meter aperture optical telescope, offering a unique platform for uninterrupted seeing-free observations across ultraviolet, visible, and infrared wavelengths from altitudes higher than 33 km. For the third flight of the upgraded SUNRISE observatory conducted in 2024, now called SUNRISE III, a new spectro-polarimeter called the Sunrise Chromospheric Infrared spectroPolarimeter (SCIP) was developed for observing near-infrared wavelength ranges around 770 nm and 850 nm. These wavelength ranges contain many spectral lines, including two of the Ca II

[1] National Astronomical Observatory of Japan, 2-21-1 Osawa, Mitaka, Tokyo 181-8588, Japan

[2] The Graduate University for Advanced Studies, SOKENDAI

[3] Department of Astronomy, Graduate School of Science, The University of Tokyo, 7-3-1 Hongo, Bunkyo-ku, Tokyo 113-0033, Japan

[4] Instituto de Astrofísica de Andalucía (IAA-CSIC), Glorieta de la Astronomía s/n, 18008 Granada, Spain

[5] Spanish Space Solar Physics Consortium, S^3PC

[6] Max-Planck-Institut für Sonnensystemforschung, Justus-von-Liebig-Weg 3, 37077 Göttingen, Germany

[7] Institute of Space and Astronautical Science, Japan Aerospace Exploration Agency, 3-1-1 Yoshinodai, Chuo-ku, Sagamihara, Kanagawa 252-5210, Japan

[8] Advanced Research Center for Space Science and Technology, Institute of Science and Engineering, Kanazawa University, Kakuma-machi, Kanazawa, Ishikawa 920-1192, Japan

[9] Institute for Space-Earth Environmental Research, Nagoya University, Furocho, Chikusa-ku, Nagoya, Aichi 464-8601, Japan

[10] National Institute of Fusion Science, 322-6 Oroshi-cho, Toki, Gihu 509-5292, Japan

[11] Kwasan and Hida Observatory, Kyoto Univ., Kurabashira, Kamitakara, Takayama, Gifu 506-1314, Japan

[12] National Solar Observatory, 22 Ohi'a Ku, Makawao, HI, 96768, USA

[13] Universitat de Valencia, Avda. de la Universitat s/n, E-46100 Burjassot, Spain

[14] Instituto de Astrofísica de Canarias, 38205 La Laguna, Tenerife, Spain

[15] Departamento de Astrofísica, Univ. de La Laguna, La Laguna, Tenerife, E-38200, Spain

[17] Instituto Nacional de Técnica Aeroespacial (INTA), Ctra. de Ajalvir, km. 4, E-28850 Torrejón de Ardoz, Spain

[16] Universidad Politécnica de Madrid, IDR/UPM, Plaza Cardenal Cisneros 3, 28040 Madrid, Spain

[18] Institut für Sonnenphysik, Schöneckstr. 6, 79104 Freiburg, Germany

[19] Johns Hopkins Applied Physics Laboratory, 11100 Johns Hopkins Road, Laurel, Maryland, USA

infrared triplet, K I D1 and D2 lines, and multiple Fe I lines, that are sensitive to solar magnetic fields and velocities in the photosphere and chromosphere. SCIP consists of a grating spectrograph in which polarimetric measurements are conducted using a rotating waveplate as a modulator and polarizing beam splitters placed in front of the cameras. The spatial and spectral resolutions are 0.21" and 1×10^5, respectively, and a polarimetric sensitivity of 0.03% (1σ) of the continuum intensity is achieved with a 10 s integration time per a resolution element. To achieve high-precision detection of small polarization signals, we carefully designed the optical and mechanical systems, polarization components, control electronics, and onboard data processing. Together with the other post-focus instrumentation developed for SUNRISE III, the SUNRISE Ultraviolet Spectropolarimeter and Imager (SUSI) and the visible imaging spectro-polarimeter Tunable Magnetograph (TuMag), SCIP provides novel observations that help elucidate energy transfer and time-dependent phenomena across the solar photosphere and chromosphere.

Keywords: balloon, near-IR, polarization, spectrograph, sun, focal-plane instrument

1. Introduction

The Sun provides a unique site to study how magnetic fields drive dynamic phenomena in astrophysical plasmas at a high spatial and temporal resolution. In addition, to understand the physical mechanisms driving the dynamics, it is critically important to obtain physical quantities, such as the temperature, velocity, and magnetic field, in a remote object using spectro-polarimetric measurements. Space-based spectro-polarimeters have been realized and provide valuable data for investigating the behavior of magnetic fields on the solar surface, i.e. the photosphere. These include the Michelson Doppler Imager (MDI: Scherrer et al. 1995) on SOHO, the Helioseismic and Magnetic Imager (HMI: Scherrer et al. 2012) on SDO, and the Polarimetric and Helioseismic Imager (PHI: Solanki et al. 2020) on Solar Orbiter, all of which provided imaging spectropolarimetry using a narrow-band tunable filter. The *Hinode* Solar Optical Telescope (SOT: Tsuneta et al. 2008) carried both a narrow-band filter imager (NFI) and a spectro-polarimeter (SP: Lites et al. 2013). The NFI provided polarimetric measurements at several photospheric and chromospheric lines with a Lyot filter (Ichimoto et al. 2008). The SP obtained spectro-polarimetric data of the Fe I lines at 630.25 nm (Landé factor $g = 2.5$) and 630.15 nm (effective Landé factor $g_{\rm eff} = 1.67$) with an echelle spectrograph and allowed us to map the magnetic fields in active and quiet regions with a spatial resolution of 0.32" owing to the diffraction-limited optical performance of a 50 cm aperture telescope and the stable observation conditions (Danilovic et al. 2008). Spectro-polarimetric observations of even larger apertures have been achieved with balloon-borne telescopes (e.g. Flare Genesis Experiment, Bernasconi et al. 2000). Among them, the SUNRISE balloon-borne solar telescope (Solanki et al. 2010; Barthol et al. 2011; Gandorfer et al. 2011; Berkefeld et al. 2011) carries a 1 m aperture optical telescope and allows

us to conduct seeing-free visible observations under stable conditions as well as UV observations with a high spatial resolution of 0.1" at wavelengths shorter than 400 nm, which cannot be well observed using ground-based telescopes due to atmospheric absorption. The Imaging Magnetograph eXperiment (IMaX) (Martínez Pillet et al. 2011) made spectro-polarimetric observations at the Fe I 525 nm line (Landé factor $g = 3$) sensitive to the solar photosphere using a narrow-band tunable filter, and provided maps of surface magnetic fields with a spatial resolution of 0.15".

In the past two flights of SUNRISE in 2009 and 2013, spectro-polarimetric observations were conducted only with IMaX in the photosphere (e.g. Lagg et al. 2010; Danilovic et al. 2010), whereas imaging observations were used to observe the overlying atmosphere, i.e., the chromosphere (e.g. Riethmüller et al. 2013; Jafarzadeh et al. 2017). There is a strong demand to expand the capability of spectro-polarimetry to conduct detailed and quantitative investigations of the chromosphere to understand the mechanisms driving the dynamic phenomena, such as jets and magneto-hydrodynamics (MHD) waves (Katsukawa 2018; Rast et al. 2021; Trujillo Bueno and del Pino Alemán 2022). Because magnetic fields in the chromosphere are generally weak and spectral lines emanating from the chromosphere are broad compared with photospheric lines, we need a high polarimetric sensitivity to obtain measurable polarization signals at a spectral line sensitive to chromospheric magnetic fields (Lagg et al. 2017; Centeno 2018). The 1 m aperture SUNRISE telescope is suitable for collecting the number of photons required for precision polarimetry and to resolve the fine-scale dynamics spatially and temporally. The third successful flight, i.e., SUNRISE III, was conducted in 2024 by upgrading the focal plane instruments (Korpi-Lagg et al. 2025) and gondola (Bernasconi et al. 2025). IMaX has been replaced by the Tunable Magnetograph (TuMag), which is able to switch the spectral lines to allow observing the mid-chromospheric line Mg I 517 nm (Quintero Noda et al. 2018b) in addition to one of the photospheric lines Fe I 525.02 nm and 525.06 nm (del Toro Iniesta et al. 2025). Observations within the UV wavelength range were conducted using the SUNRISE Filter Imager (SuFI) during previous flights (Gandorfer et al. 2011). It has been replaced with the SUNRISE UV Spectropolarimeter and Imager (SUSI) in SUNRISE III to make spectro-polarimetric observations within the wavelength range of 309 – 417 nm (Feller et al. 2025). The Correlating Wavefront Sensor (CWS), as flown in the previous flights, is an instrument for tip-tilt mirror compensation of image motions, for closed-loop autofocus, and for measuring low-order aberrations for better image stability and quality (Berkefeld et al. 2026).

In addition to the above three instruments, a new instrument called the Sunrise Chromospheric Infrared spectroPolarimeter (SCIP) has been newly developed to observe near-infrared spectral lines sensitive to solar magnetic fields in both the photosphere and the chromosphere. The SCIP instrument was designed and built through international collaboration among Japanese institutes including the Japan Aerospace Exploration Agency (JAXA), the Spanish Space Solar Physics Consortium (S^3PC) led by the Instituto de Astrofísica de Andalucía (IAA-CSIC), and the German Max Planck Institute for Solar System Research (MPS) with the leadership of the National Astronomical Observatory of Japan (NAOJ).

2. Concepts of SCIP

2.1. Science targets and requirements

The science targets of SCIP are to (1) determine the 3D magnetic structure from the photosphere to the chromosphere, (2) trace MHD waves from the photosphere to the chromosphere, and (3) reveal the mechanisms driving chromospheric jets, by measuring the height- and time-dependent velocities and magnetic fields in the solar atmosphere (Figure 1). To achieve them, SCIP is designed to observe two spectral regions centered at 850 and 770 nm in the near-infrared wavelength range (Figure 2). The two wavelength ranges contain many spectral lines that produce measurable polarization signals through the Zeeman effect in the presence of magnetic fields. In particular, the Ca II lines at 849.8 nm (effective Landé factor $g_{\rm eff} = 1.07$) and 854.2 nm ($g_{\rm eff} = 1.10$) are sensitive to magnetic fields in the chromosphere (Quintero Noda et al. 2017a). The K I lines at 766.4 nm ($g_{\rm eff} = 1.16$) and 769.9 nm ($g_{\rm eff} = 1.33$) are sensitive to the atmosphere at the interface between the photosphere and the chromosphere (Quintero Noda et al. 2017c). There are multiple spectral lines sensitive to the photosphere, such as the Fe I 846.8 nm line (Landé factor $g = 2.5$), within the wavelength range. By combining these spectral lines, we can seamlessly cover the photosphere and the chromosphere and obtain 3D magnetic and velocity structures in the solar atmosphere, as shown in Figure 3. It has been demonstrated that spectro-polarimetric observations of these lines provide a good diagnostic tool to understand the mechanisms driving dynamical processes, such as jets, MHD waves (Quintero Noda et al. 2017b, 2019; Matsumoto et al. 2023), and magnetic reconnection (Kawabata et al. 2024). It is worth noting that the 770 nm band is heavily affected by the O_2 band in the Earth's atmosphere. In particular, the K I 766.4 nm line is completely absorbed by an O_2 line, so neither its intensity nor polarization profiles can be measured with a ground-based telescope. At the balloon altitude, the absorption becomes much weaker, enabling a reliable measurement of the polarization profile of the K I 766.4 nm line for the first time (Quintero Noda et al. 2018a).

In addition to the spectral coverage, a high spatial resolution is also required to resolve the dynamic phenomena occurring in the atmosphere, where we set a goal to achieve a spatial resolution of 0.21" (corresponding to about 150 km on the solar surface), which is the diffraction-limit of the 1 m aperture telescope at a wavelength of 850 nm. A polarimetric sensitivity of 0.03% (1σ) of the continuum intensity is necessary to measure weak polarization signals in the chromospheric lines, such as Ca II 854.2 nm and 849.8 nm. By combining the 1 m aperture telescope with optimized optical elements and high polarization modulation efficiencies, we aim to achieve the polarimetric sensitivity within a resolution element smaller than 0.2" in less than 10 s of integration time. This is critical for obtaining the temporal evolution of magnetic fields that drive dynamics with lifetime as short as 10 s (e.g. Wedemeyer-Böhm, Lagg, and Nordlund 2009). To sample multiple wavelength points across narrow photospheric lines and distinguish the polarization (Stokes) spectral profiles, a spectral resolution higher than 1×10^5 is required. The field-of-view (FoV) is limited by the upstream optics but

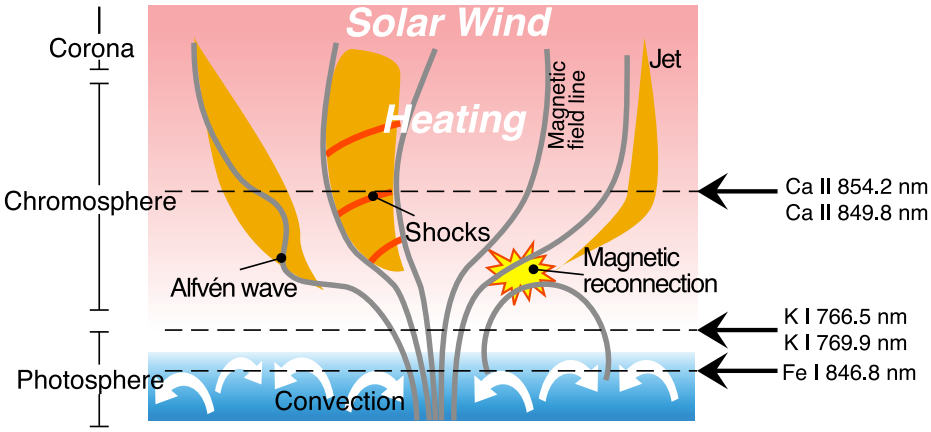


Figure 1. Science targets using SCIP. Spectro-polarimetric measurements of multiple spectral lines from the photosphere to the chromosphere allow us to obtain three-dimensional structures of magnetic and velocity fields and reveal the nature of the jets and MHD waves responsible for heating the atmosphere and acceleration of the solar wind. Modified from Katsukawa et al. (2020).

is required to be larger than 50"×50". Seeing-free observations achieved using the stratospheric balloon-borne telescope allow us to map magnetic structures and their temporal evolution in the solar atmosphere with good spatial and spectral resolution, along with the polarimetric sensitivity described above. The key requirements are summarized below.

- Wavelength coverage to include spectral lines, allowing seamless coverage of the photosphere and the chromosphere (Figure 3).
  - Two wavelength bands including Ca II 850 nm and K I 770 nm lines (Figure 2)
- Spatial and temporal resolution high enough to resolve fine-scale dynamics in the chromosphere.
  - Spatial resolution of 0.21" (diffraction limit resolution at 850 nm)
  - Stokes IQUV (normal mode): temporal resolution shorter than 10 sec at each slit position
  - Stokes I only (rapid mode): temporal resolution shorter than 45 sec for scanning a full FoV
- Spectral resolution and polarization sensitivity sufficiently high to get polarization signals at the photospheric and chromospheric spectral lines
  - Spectral resolution and sampling larger than $\lambda/\Delta\lambda = 1 \times 10^5$ and 2×10^5, respectively
  - Polarization sensitivity of 0.03% (1σ) of the continuum intensity
- Field-of-view large enough to cover a super-granular scale
  - 58"×58"

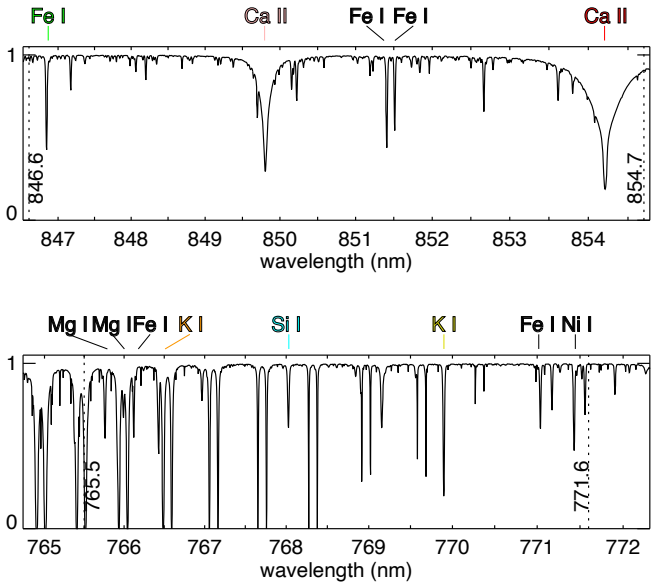


Figure 2. Atlas spectra of the two SCIP spectral windows, (top) 850 nm and (bottom) 770 nm windows, and key spectral lines in the wavelength ranges. This solar spectral atlas shown here is compiled using data from the NSO FTS flux atlas (Kurucz et al. 1984).

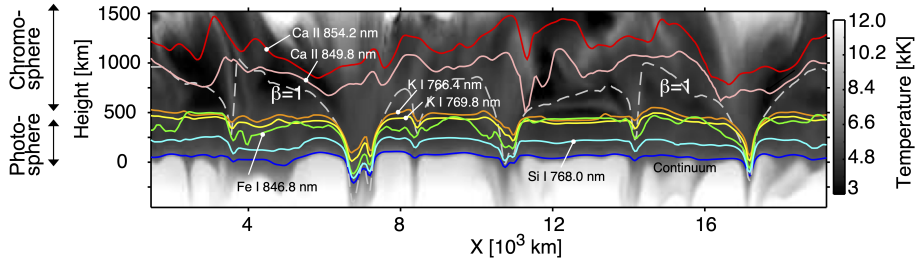


Figure 3. Formation heights of key spectral lines observed with SCIP, including Ca II 854.2 nm and 849.8 nm, K I 766.4 nm and 769.9 nm, Fe I 846.8 nm, and Si I 768.0 nm. The figure was made using a 3D MHD simulation and non-LTE radiative transfer calculation (Quintero Noda et al. 2017c). The gray scale represents temperatures within the solar atmosphere. Modified from Katsukawa et al. (2020).

2.2. SCIP instrument overview

SCIP consists of two major units: the Optics unit (O-unit) and the Electronics unit (E-unit) (Katsukawa et al. 2020). The O-unit contains optical components and cameras and is installed in the Post Focus Instrumentation (PFI) structure (see Section 3 for details). The E-unit contains control electronics and is installed in the gondola E-rack (see Section 4 for details). The spectro-polarimeter (SP) of the SCIP O-unit is a long-slit spectrograph that uses an echelle grating to observe two wavelength ranges around 850 nm and 770 nm (Figure 4). A slit-jaw (SJ) optics system is used to observe a 2D image around the slit and consists of a reflective filter and a doublet lens unit. The reflective filter transmits

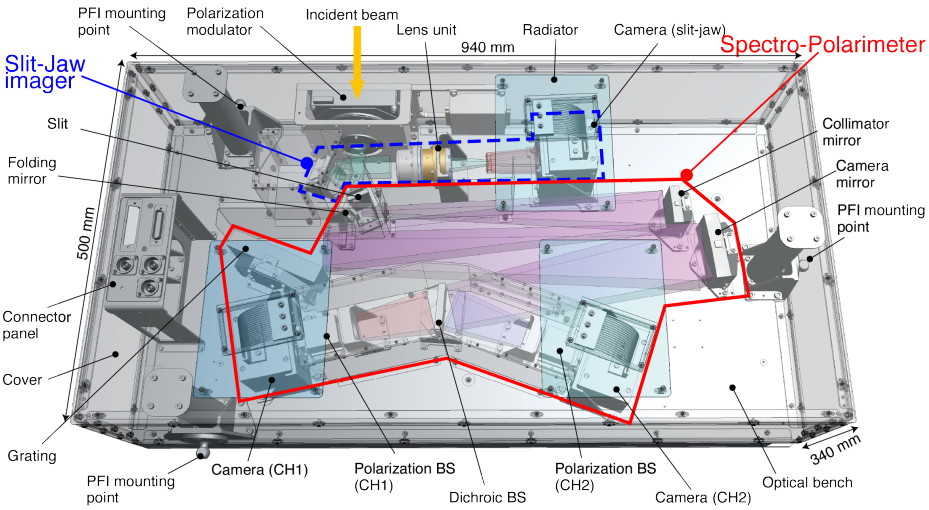


Figure 4. The opto-mechanical layout of the SCIP O-unit. The cover and the lighttrap structures are shown as transparent for clarity. Modified from Uraguchi et al. (2023).

unnecessary passband light to a light trap behind the filter. Details of the optical and mechanical designs are described in Sections 3.1 and 3.2, respectively. We use three cameras (850 nm, 770 nm, and SJ) employing a back-side illuminated CMOS sensor, with electronics newly developed for SUNRISE III (see Section 3.5 for details).

The polarimetric measurement is carried out by the combination of a rotating waveplate located at the optical entrance of the O-unit and the polarization beam splitters (PBSs) located in front of the cameras (Section 3.3). The rotating waveplate creates a temporally modulated solar image on the slit. Because there are multiple folding mirrors in the telescope and Image Stabilization and Light Distribution unit (ISLID) feeding the light into the O-unit, we need not only an instrument-level, i.e., SCIP only, polarization calibration but also end-to-end polarization calibration combined with the telescope and ISLID after we mount the SCIP O-unit onto the PFI structure. Details of the polarization calibration are described in Section 6.3.

Figure 5 shows a block diagram of the SCIP O-unit and E-unit with associated electronics components. For accurate polarization measurements, it is important to achieve a good synchronization between the exposures by the cameras and the rotating phase of the waveplate by a polarization modulation unit (PMU) (Kubo et al. 2020, see Section 3.3 for details). The E-unit, along with onboard software and firmware, achieves synchronization and control of the O-unit in the following way:

- The PMU sends phase signals to the E-unit. Exposures of the three cameras are triggered by the phase signals, and the E-unit sends an exposure command to the cameras.
- The E-unit receives images taken by the three cameras and applies onboard image processing, including polarization demodulation, in which accumula-

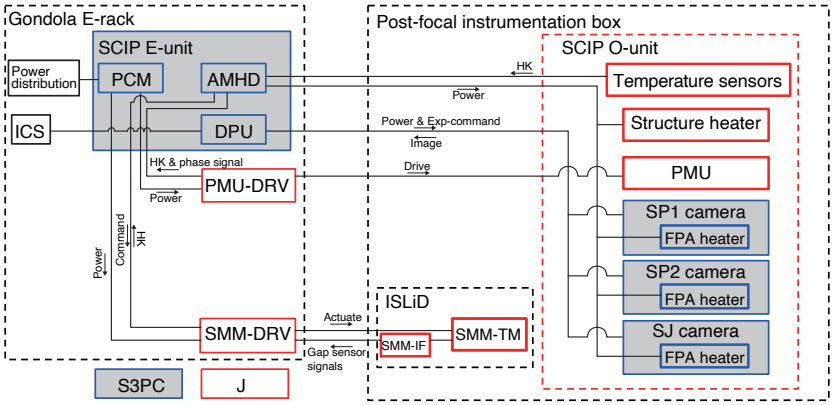


Figure 5. Block diagram of the SCIP electronics for observation control. The control electronics of the SCIP E-unit are located on the gondola E-rack. The driver electronics boxes for the PMU and SMM are also located on the E-rack and controlled by the E-unit. Exposures of the three cameras are triggered by phase signals generated by the PMU, and the E-unit sends an exposure command to the cameras. The E-unit receives images taken by the three cameras and applies onboard image processing. The E-unit also sends a command to the SMM to move the scan mirror. Structure and camera heaters are placed inside the O-unit to stabilize the temperature environment of the O-unit. The red boxes indicate components developed by the Japanese team, whereas the blue boxes indicate components developed by the S^{3}PC. Modified from Katsukawa et al. (2020).

tion and subtraction of the images are achieved depending on the rotating phase of the waveplate (See Section 5 and Appendix A).

- The E-unit synchronizes the scan mirror mechanism (SMM), which scans perpendicular to the slit, with the PMU rotation and camera exposures to prevent image motion during exposure (see Section 3.4 for details on SMM).
- The E-unit controls the heaters and collects temperature data from sensors distributed in the O-unit.

3. SCIP O-unit

The SCIP O-unit contains the optical system for spectro-polarimetric observations using the slit spectrograph and for imaging observations using the slit-jaw optical system. This section describes the optical, mechanical, and thermal designs of the O-unit and its accompanying electrical components: the PMU, SMM, and cameras.

3.1. Optical design

3.1.1. SP optics

SUNRISE employs a 1 m aperture telescope with a Gregorian design. It feeds light into ISLiD. The ISLiD system of SUNRISE I and II (Gandorfer et al. 2011) was completely redesigned for SUNRISE III to accommodate the new instrument

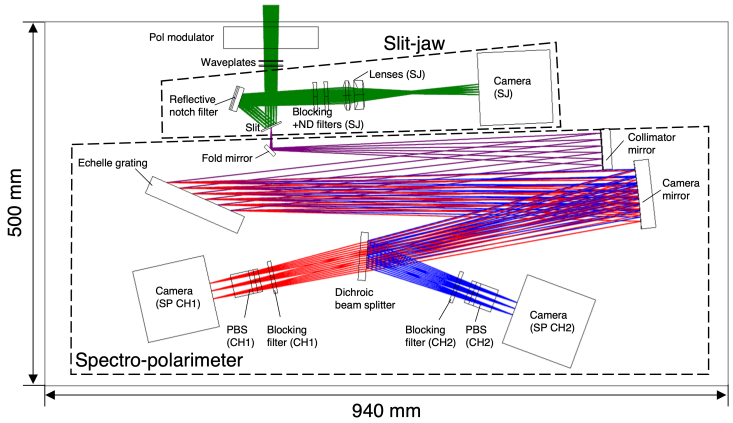


Figure 6. Layout of the SCIP optics. The colors of the rays represent the following: (red) SP CH1, (blue) SP CH2, and (green) SJ. Modified from Tsuzuki et al. (2020).

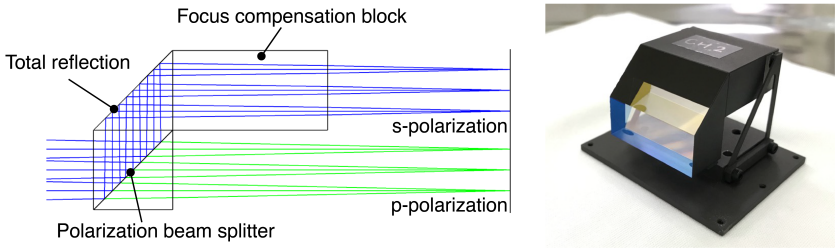


Figure 7. (left) Optical design of the PBS, using a cube beam splitter with a dielectric coating at the 45° surface, and with anti-reflection coatings on the entrance and exit surfaces. To adjust the focus position, a glass block is inserted in the optical path of the s-polarization that is reflected at the 45° surface. The thickness of the glass block is designed to make s- and p-polarizations in focus on the same plane. (right) Picture of the PBS for the 770 nm wavelength band (CH2). Modified from Tsuzuki et al. (2020).

SCIP in addition to SUSI, TuMag, and CWS. The new ISLiD, described in Korpi-Lagg et al. (2025), consists of two Offner relay optical systems (Smith 2007) that transfer the Gregorian focus (F2) to the instruments. The first Offner system, consisting of the two spherical mirrors M5 and M6 feeds light into SUSI, TuMag, and CWS by dichroic beam splitters. M6 is used as a tip-tilt mirror for correlation tracking driven by CWS. The second Offner system, consisting of two spherical mirrors M7 and M8 with three folding mirrors (M9, M10, and M11), is used to feed the F/24.2 beam into SCIP. One of the spherical mirrors, M8, is mounted on a scan mirror mechanism (SMM) and is used by SCIP to scan a FoV perpendicular to the slit (see Section 3.4).

The SCIP optical layout is shown in Figure 6 by the red and blue lines. The incident convergent light of F/24.2 first passes through the rotating waveplates and reaches the slit. The SP uses light passing through the slit. The light transmitted through the slit spreads out more in the direction perpendicular to the slit (i.e., dispersion direction) due to diffraction. Because the observing wavelength is in the near-infrared and longer than visible light, we need to take

into account the effect of diffraction caused by the 11 μm-wide slit. In the optical design after the slit, we use the F/11 beam in the direction perpendicular to the slit, while the F/24.2 beam is used in the direction parallel to the slit. The energy contained in the F/11 beam is larger than 85% at both 850 nm and 770 nm.

The SP optics is based on the modified Czerny-Turner mounting comprising an echelle grating and two mirrors (collimator and camera mirrors) in a quasi-Littrow configuration. The light from the slit is collimated by the collimator mirror and impinges on the grating. The collimated light is diffracted by the echelle grating with a groove density of 110/mm, so that the two wavelength bands are observed simultaneously using different diffraction orders: the 19th order to observe the 850 nm wavelength band (CH1), and the 21st order to observe the 770 nm wavelength band (CH2). The grating has a blaze angle of 64°, but the angle of incidence to the grating was designed to be 59.6° to maintain the clearance between the collimator mirror and the camera mirror. The diffracted parallel light from the echelle grating becomes converging light by the camera mirror. In order to achieve high imaging performance, the mirror surface shapes of the collimator and camera mirrors were determined by optimization. These surface shapes are similar to off-axis parabolas but include higher-order aspheric terms to sufficiently suppress the aberration (see details in Tsuzuki et al. 2020).

The two wavelength bands are split by a dichroic filter with a long-pass coating. In each channel, the required wavelength bands are extracted through a blocking filter. For simultaneous observation of two orthogonal linear polarizations, a PBS is placed in front of each detector, which creates the orthogonal polarization images on each single detector (Figure 7). The PBS has an extinction ratio specification of more than 100, as verified by the vendor Nitto Optical. Figure 8 shows RMS wavefront errors of the SP optics based on the optical design, which shows that the worst wavefront error is 4.6 nm rms as a design performance in the two channels. The total wavefront error, considering fabrication and alignment errors, is estimated to be 48 nm rms from a tolerance analysis (Tsuzuki et al. 2020). The optical parameters of the SP are summarized in Table 1. Pictures of the optical elements and their mounting structures are shown in Figure 9.

3.1.2. SP throughput for polarimetric measurements

To achieve a high polarization sensitivity, we have to collect sufficient photons within the integration time. When considering (1) the reflectances and transmittances of all the optical components, including the telescope, ISLiD, and the SCIP O-unit, and (2) the quantum efficiency of the image sensor, the total efficiency of the system is 2.4% and 4.8% in the 850 and 770 nm bands, respectively. The worse efficiency at 850 nm is because the mirrors in the telescope and the first half of ISLiD have an aluminum coating on the reflecting surfaces to observe the UV wavelengths (Feller et al. 2025), but this coating has lower reflectivity around 850 nm. The image sensor (see Section 3.5) is also less sensitive to 850 nm. The number of detected electrons is estimated to be 1.1×10^6 e/(pixel·s) and 2.3×10^6 e/(pixel·s) at continuum wavelenghts around

Table 1. SCIP SP optical parameters

Basic features	
Spectrograph type	Modified Czerny-Turner in quasi-Littrow configuration
FOV	11 μm (0.094", slit width)×6.8 mm (58", slit length)
Wavelength range	(CH1): 846.830–854.930 nm (in vacuum, 19th order)
	(CH2): 765.708–771.808 nm (in vacuum, 21st order)
Plate scale (spatial)	0.0935"/pixel
Plate scale (dispersion)	(CH1) 42.3 mÅ/pixel at 846.6 nm (R=2×10^5)
	(CH2) 38.5 mÅ/pixel at 765.5 nm
Opt. elements	**Features and specifications**
Waveplate#1	Plane parallel plate (t=1.43 mm), quartz
Waveplate#2	Plane parallel plate (t=1.64 mm), sapphire
Slit	Width: 11 μm (corresponding to 0.0936")
	Length: 6.8 mm (corresponding to 58")
	Plane parallel plate (t=2 mm), fused silica
	25° to the incident optical axis from ISLiD
Folding mirror	Planar, fused silica
Collimator mirror	Spherical plus XY polynomial, CLEARCERAM-Z
	Curvature radius R=1060.6 mm
	Protected silver coating
Grating	COTS grating by Richardson Gratings™, Newport
	Planar constant-line-space grating, ZERODUR
	Groove density 110/mm, blaze angle 64°
	Angle of incidence 59.6°relative to the grating normal
	Protected silver coating
	Clear aperture: 46 mm×130 mm
Camera mirror	Spherical plus XY polynomial, CLEARCERAM-Z
	Curvature radius R=1060.8 mm
	Protected silver coating
Dichroic beam splitter	Reflectivity> 98% in $\lambda = 760 - 780$ nm
	Transmission> 98.5% in $\lambda = 840 - 860$ nm
	Specified for an angle of incidence (AOI) of $12 - 21°$ for both s- and p-polarizations.
	Wedged plate (t=10 mm), fused silica
	Wedge angle 0.176° relative to the front surface
Blocking filters	Bandpass: 10.9 nm around 850.75 nm (CH1), 9.9 nm around 768.55 nm (CH2)
	Plane parallel plate (t=5 mm), fused silica
PBSs	13 mm block prism, BSL7Y
	Comp. block thickness 25.49 mm (CH1) and 25.41 mm (CH2)
Camera sensor	2048×2048 pixels, 11 μm/pixel

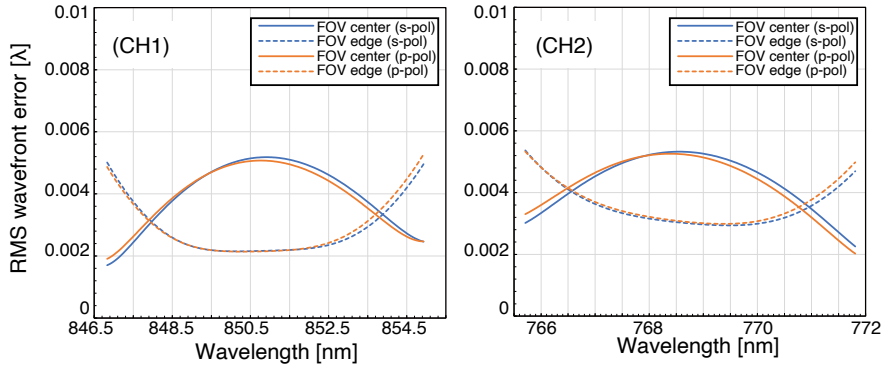


Figure 8. RMS wavefront error of SP as a function of the wavelength for the 850 nm channel (CH1; left) and 770 nm channel (CH2; right). The plots show the wavefront errors at the center and edges of the FoV for both s- and p-polarizations. Modified from Tsuzuki et al. (2020).

850 and 770 nm, respectively, in a solar disk center observation. Because the full-well capacity of the image sensor is $\sim 9 \times 10^4$ e, each exposure should be shorter than 32 ms. To achieve a polarimetric sensitivity of 0.03% (1σ) of the continuum intensity, a 10 sec image accumulation, combining s- and p-polarization beams, and binning over two pixels (0.19" sampling) along the slit are required in the 850 nm band, given the polarization modulation efficiency, whereas no summing is needed in the 770 nm band.

3.1.3. SJ optics

The SJ optical layout is shown in Figure 6 with the green lines. The SJ observes light reflected by the slit plane, which first reaches a reflective filter with a notch filter coating to reflect the wavelength of 770.5±30 nm (FWHM) on the front side and transmits unwanted wavelengths. The transmitted unwanted light has a large energy compared to the reflected light and is attenuated by a black baffle around the filter. The rear surface of the reflective filter has a wedge to deflect the unwanted light. The light reflected from the reflective filter is then passed through an SJ blocking filter to extract only the required wavelength band of the continuum wavelength at 770.7±0.5 nm (FWHM). The light passing through the filter then enters the doublet lens, which forms a 1× magnified image of the slit plane on the detector. Since the SJ has a sufficiently narrow wavelength band, the doublet lens is able to achieve adequate imaging performance with the same glass material, instead of multiple materials required for chromatic aberration correction. We selected BSL7Y (OHARA Inc.) as the lens material. The FoV is 64"×64", with a pixel scale of 0.0936"/pixel. The optical parameters of the SJ are shown in Table 2. The worst wavefront error is 3.5 nm rms as a design performance in the FoV. The total wavefront error, considering fabrication and alignment errors, is estimated to be 34 nm rms by the tolerance analysis (Tsuzuki et al. 2020).

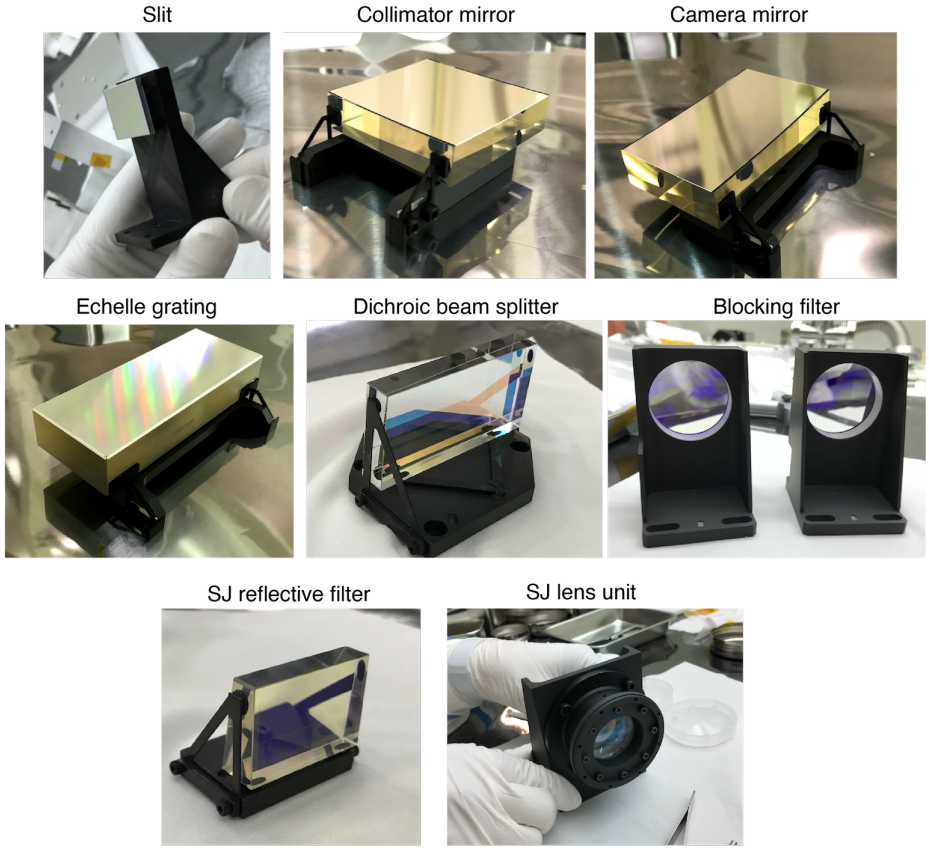


Figure 9. Optical elements and their mounting structures in the SCIP O-unit.

3.2. Opto-mechanical design

Figure 4 shows the opto-mechanical layout of the SCIP O-unit. All optical components are mounted on an optical bench consisting of a carbon fiber reinforced plastic (CFRP)-aluminum-honeycomb sandwich panel. To meet the strict wavefront error requirements for high spatial and spectral resolution, the optical elements are held by supporting mechanisms that minimize deformation of the optical surfaces. The CFRP sandwich panel offers significant advantages in low thermal deformation, weight and stiffness. The coefficient of thermal expansion (CTE) of the CFRP sandwich panels was measured using a test piece of the panel, yielding -0.15 ppm/K and 0.4 ppm/K in the two in-plane directions. Deformation due to moisture desorption was also measured and was found to be less than 5 ppm over 7 days. Note that the CTE in the out-of-plane direction does not need to be considered because it does not affect the relative position and orientation of the optics on the bench (Uraguchi et al. 2020).

The reflective and diffractive optical elements (collimator and camera mirrors, and grating) are supported by a quasi-kinematic mount consisting of flexures at its top and bottom surfaces, as shown in Figure 10(a). The thickness of the

Table 2. SCIP SJ optical parameters

Basic features	
Imaging optics	Doublet (air-spaced two lenses)
FOV	7.6 mm×7.6 mm (64"×64")
Wavelength band	770.208–771.208 nm (in vacuum)
Plate scale	0.0936"/pixel
Magnification	1.0
Opt. elements	**Features and parameters**
SJ reflective filter	Bandpass: 770.5±30 nm (FWHM)
	Wedged plate (t=9 mm), CLEARCERAM
	9.0° wedge relative to the front surface
SJ blocking filter	Bandpass: 770.5±0.5 nm (FWHM)
	Plane parallel plate (t=5 mm), BK7
SJ ND filter	Plane parallel plate (t=5 mm), BK7
SJ lens#1	Bi-convex spherical lens (t=12 mm), BSL7Y
	Curvature radii R1=48.646 mm, R2=62.758 mm
SJ lens#2	Meniscus spherical lens (t=8 mm), BSL7Y
	Curvature radii R1=36.294 mm, R2=112.642 mm
Camera sensor	Same as SP

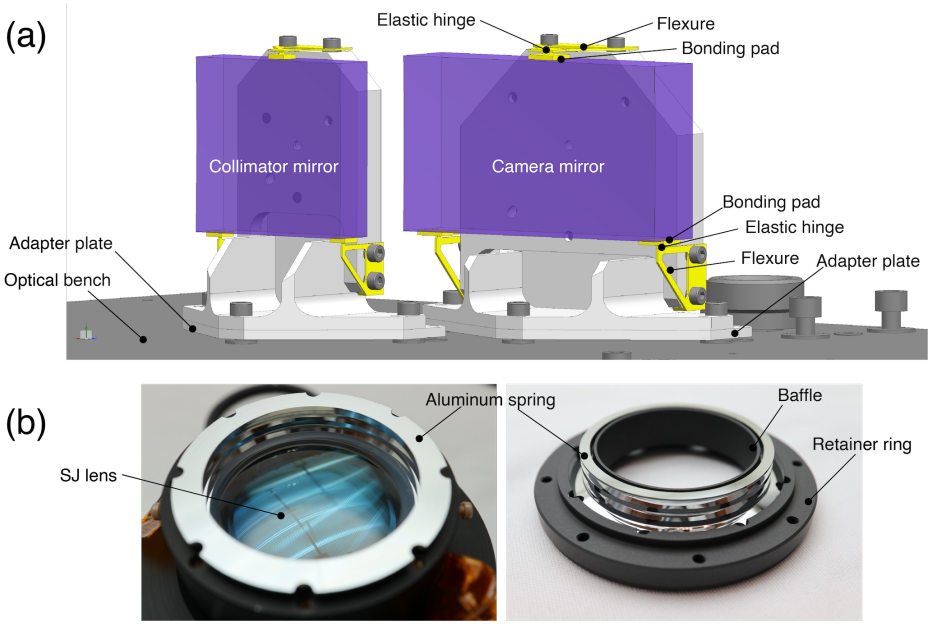


Figure 10. (a) Illustration of the mirror support mechanisms for the collimator and camera mirrors. (b) Aluminum spring inserted into the SJ lens barrel (left) and the retainer ring (right). Modified from Uraguchi et al. (2020).

flexure is set to 0.5 to 0.9 mm, i.e. as thin as possible to avoid inducing surface deformation while meeting the required mechanical tolerances. The flexure includes a monolithically machined bonding pad connected by elastic hinges with cross-sections ranging from 0.5×0.5 mm square to 1×1 mm square to provide the appropriate rotational degree of freedom. The optical element is bonded to the pad with an adhesive. The adhesive areas range from 6×6 mm square to 8×20 mm rectangular to adapt to the sizes and the masses of the substrates, and the adhesive layer thickness is commonly set to 0.15 ± 0.05 mm. The mirror substrate is also designed to minimize the surface deformation due to mounting. The thickness of the substrate is set to greater than 1/6 of the diagonal dimension of the substrate to ensure a sufficient area on the side faces for bonding. In addition, 5 mm margins are provided on the adhesive side at the top and bottom surfaces to reduce the effect of adhesion on the clear aperture. The material of the flexure pad is selected to match the CTE of the substrate material to the extent possible. The super invar alloy is used for CLEARCERAM-Z, fused silica, and ZERODUR, and the titanium alloy is used for BSL7Y.

The refractive optical elements, such as waveplates, SP and SJ blocking filters, and SJ lenses, are held by a preloaded spring made of polytetrafluoroethylene (PTFE) or aluminum (Figure 10 [b]). The springs are not only to apply the preload to avoid separation at the expected accelerations but also to absorb the thermal strain difference between the mounting structure and the substrate. Figure 10(b) shows a metal spring made of aluminum alloy 6061 used for the SJ lenses. This aluminum spring has a 0.15 mm thick bellows-like cross-section that provides good mechanical stability and thermal conductivity compared with the PTFE springs. The mounting structures fabricated are shown in Figure 9.

Figure 11 shows pictures of the SCIP O-unit at various stages of the integration process. Some optical elements and paths are covered by the light-trap structures to suppress stray light in the O-unit as specified in Tsuzuki et al. (2020). Blackening by plasma electrolytic oxidation (PEO) is applied to the aluminum light-trap structures. The O-unit is enclosed by a thin CFRP plate to minimize thermo-elastic deformation while maintaining sufficient stiffness and reducing weight. The SCIP O-unit has a mass of 27 kg in its flight configuration.

Integration of the SCIP O-unit into the PFI is done through the three mount interface devices, which provide point fixation, line fixation, and flat fixation to constitute a kinematic mount that ensures the appropriate degrees of freedom to avoid over-constraining the O-unit. The point fixation device is located at the point closest to the optical interface, the line fixation device is aligned along the incident optical axis, and the flat fixation is applied to the remaining interface point.

To demonstrate that the opto-mechanical design of the O-unit meets the required wavefront error budget, it is necessary to quantify the errors due to environmental effects such as gravity and temperature variation under the observation conditions. We conducted an integrated opto-mechanical analysis by (1) incorporating mechanical and thermal disturbances into a finite element model of the O-unit to obtain the nodal displacements of each optical element, (2) feeding them into the optical analysis in the form of rigid-body displacement and surface deformation fitted by polynomials, and (3) analyzing wavefront errors of the SP

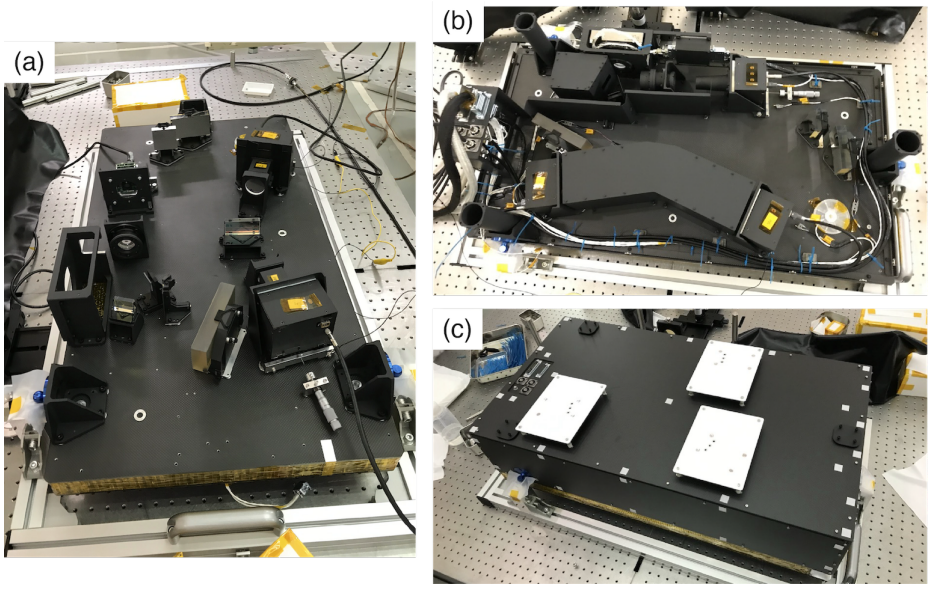


Figure 11. Pictures of the SCIP O-unit (a) before installing the light trap structures, in which the SJ camera is not installed yet, (b) after installation of the light-trap structure around the SP cameras and SJ reflective filter as well as the SJ camera baffle, and (c) after installation of the CFRP enclosure and the camera radiators.

and SJ optical systems (Uraguchi et al. 2020, 2023). The analyses showed that mounting and environmental effects caused wavefront errors of less than 2 nm rms and 8 nm rms, respectively, for the SP, which is well within the wavefront error budget provided by Tsuzuki et al. (2020). The opto-mechanical effects on wavefront errors were much smaller for the SJ than for the SP. The analysis also explained changes of the image position observed in the thermal vacuum optical test (see Section 6.4.1).

3.3. Polarization modulation

The polarization measurements are done by a combination of a rotating waveplate, PBSs (Section 3.1), and cameras (Section 3.5) in the SCIP O-unit. The SCIP O-unit uses a polarization modulation unit (PMU) to continuously rotate a waveplate at a constant speed. The PMU consists of (1) a rotating mechanism (PMU-ROT), (2) its driver electronics (PMU-DRV), and (3) filter electronics (PMU-IF), as shown in Figure 12. The PMU-ROT and PMU-IF are installed in the SCIP O-unit as one of the components. The PMU-DRV is installed in the gondola E-rack (Figure 5). Table 3 summarizes the characteristics of the PMU. The rotating mechanism PMU-ROT uses a DC brushless motor which was originally developed as a breadboard mechanism to evaluate its performance for future solar observations by a large-aperture optical telescope on a spacecraft (Shimizu et al. 2014). The mechanism provided a successful supreme performance exceeding 10 million times of continuous rotations in a lifetime testing under a high vacuum thermal environment over three years. After the lifetime

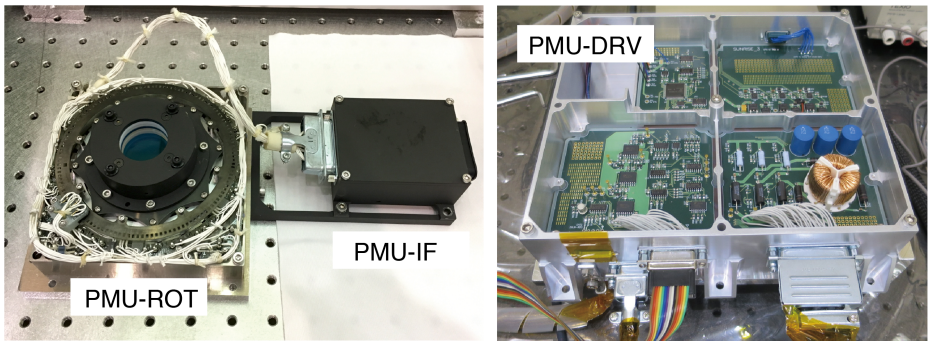


Figure 12. (left) The rotating mechanism of the waveplate (PMU-ROT) and its filter electronics (PMU-IF) which are installed in the SCIP O-unit. (right) The driver electronics (PMU-DRV) for the PMU-ROT, which is installed in the gondola E-rack. Modified from Kubo et al. (2020).

test, it was adopted for the polarization modulation on the SCIP instrument (Shimizu et al. 2018). Thus, the mechanism may not be optimally designed, as the diameter of the hollow aperture (68 mm) is much larger than necessary for the beam size entering the waveplate. The PMU-IF is added to reduce noise in the encoder signals for the rotational phase from the PMU-ROT. Since the spatial resolution of SCIP is approximately 10 times higher than that of the CLASP rocket experiment, which used the same type of rotating mechanism (Ishikawa et al. 2015), the rotation speed of the PMU-ROT must be approximately 10 times faster than that of CLASP (4.8 sec/rotation) to suppress polarization crosstalk due to platform jitter when observing the fine-scale dynamics in the solar atmosphere. The driver electronics PMU-DRV was newly developed to make it optimized for the rotation speed of 0.512 sec/rotation. Another set of the same rotating mechanism and its driver electronics was manufactured and installed in the Sunrise UV Spectropolarimeter and Imager (SUSI) for UV spectropolarimetry (Feller et al. 2025).

The camera operations are synchronized with phase signals sent from the PMU-DRV, performing an exposure every 22.5° in modulator angle and having 16 images during one rotation of the waveplate. The full Stokes vector is obtained by onboard polarization demodulation by the SCIP E-unit, which uses an integration of the acquired images multiplied by coefficients according to the rotational phase of the waveplate (Kubo et al. 2023). If the waveplate does not rotate uniformly or the camera exposure is out of synchronization, polarization errors are induced by the difference in the rotational phase between the polarization modulation and polarization demodulation. We developed the control logic in the PMU-DRV to achieve the required rotation uniformity with a speed of 0.512 sec/rotation. The polarization modulation was optically measured by mounting a non-flight half-waveplate simulating the same mass and inertia, demonstrating that the rotation angle errors derived were within $\pm 1°$ by the encoder signals and the optical measurement. Figure 13 (a) shows the frequency dependence of the rotation angle errors averaged over 500 rotations to verify that the rotation angle error at each cycle is within the requirement determined

Table 3. Basic features of PMU mechanism and the waveplate

Mechanism	
Rotating mechanism	DC brushless motor
Waveplate rotation speed	0.512 sec/rotation
Number of exposures	16 exposures/rotation
Angle error	$\pm 1^\circ$
Waveplate	
Material	quartz and sapphire
Wavelength	762–775 nm, 842–859 nm
Retardation	$127^\circ \pm 3^\circ$
Diameter	ϕ30 mm
Clear aperture	ϕ27 mm
Parallelism	2" for each plate
Transmission wavefront error	$\lambda/15$ PV for each plate
AR Coating	Reflectivity $< 1\%$ on both sides

by the polarization accuracy. The angle errors are below the requirement except for $n = 0$ and 2 cycles. The rotation angle error at $n = 2$ cycles exceeds the requirement but is within the tolerance. The polarization error due to $n = 0$ cycles appears as a crosstalk between Stokes Q and U and can be corrected using housekeeping encoder data even after the onboard demodulation. Details of the tests and their results are provided in Kubo et al. (2020) and Kubo et al. (2021).

As stated in Section 3.1, the waveplate used in SCIP consists of a quartz (SiO_2) and sapphire (Al_2O_3) plates. The combination was selected because it can cancel the wavelength dependence and temperature dependence of the retardation over a wide wavelength range. The thickness of the quartz and sapphire plate is designed so that the retardation is close to 127° to have good polarization modulation efficiency for both the circular and linear polarization. The two plates are independently mounted in the waveplate holder by PTFE springs, considering different CTE. Anti-reflective coatings are applied on both sides to avoid multiple reflections between the two plates. Table 3 summarizes the specifications of the waveplate. The temperature dependence of the retardation was measured using a prototype of the waveplate consisting of the same material (Kubo et al. 2020). Figure 13 (b) shows the measured retardation as a function of the wavelength at various temperatures from 7°C to 37°C, demonstrating that the change in the retardation is as small as $\pm 1^\circ$ when the temperature is maintained at 20 ± 5°C (see Section 3.6 for details on O-unit thermal control). In the flight waveplate, the optical axes of the quartz and sapphire plates were carefully aligned by rotating one of the plates to suppress ripples seen in the prototype waveplate. After the final adjustment, the retardation of the flight waveplate is almost constant at 125.5° in the two wavelength bands as shown in Figure 13 (c). The beam wobbling by the waveplate rotation was minimized by

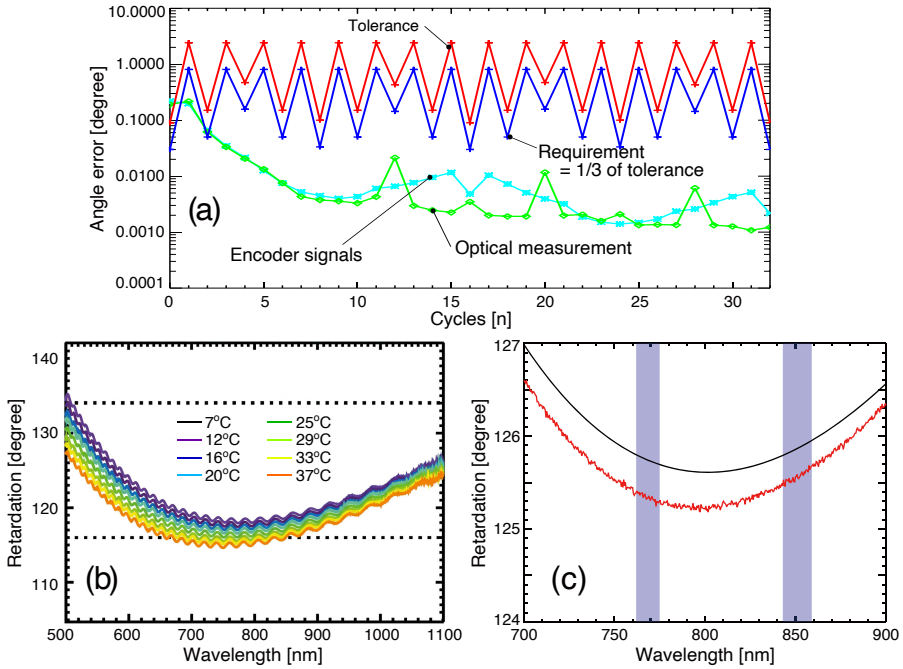


Figure 13. (a)Rotation angle error as a function of the cycle in one rotation, in which the red and blue lines show tolerance coming from the required polarization accuracy and requirements allocated to each cycle component defined by 1/3 of the tolerance (Kubo et al. 2020). The green and light blue lines show optical and encoder measurements of the angle errors, respectively. (b) Temperature dependence of the retardation angle for a prototype waveplate consisting of quartz and sapphire plates, with temperatures indicated by different colors. (c) Wavelength dependence of the retardation for the flight waveplate, in which the black and red lines show designed and measured (at 23°C) retardation, respectively. Modified from Kubo et al. (2020).

adjusting the tilt of the waveplate relative to the rotating axis of the mechanism using shims and is smaller than 0.01″ root-mean-square (rms).

3.4. Scan mirror

Because the SCIP O-unit provides a single-slit spectrograph, a scan mirror mechanism (SMM) is required to map a two-dimensional FoV by tilting a mirror. The SMM consists of three units: a tip-tilt mirror mechanism (SMM-TM), electronics that control a mirror tilt (SMM-DRV), and an electrical unit reading the output signals from gap-based capacitance sensors installed in the tip-tilt mirror (SMM-IF), as shown in Figure 14 (Oba et al. 2020, 2022). The SCIP E-unit transmits a tilt command to the SMM-DRV that drives a tip-tilt motion of the SMM-TM. The SMM operations are synchronized by the E-unit using the PMU phase signals, as well as the camera operations (Section 3.3). The E-unit triggers a camera exposure 32 ms later than the timing of the tip-tilt command to avoid an exposure during mirror motion. This means the mirror tilt has to be moved and stabilized within 32 ms after the tilt command. Table 4 summarizes the basic features of the SMM. The SMM-TM and SMM-IF are installed not in the SCIP

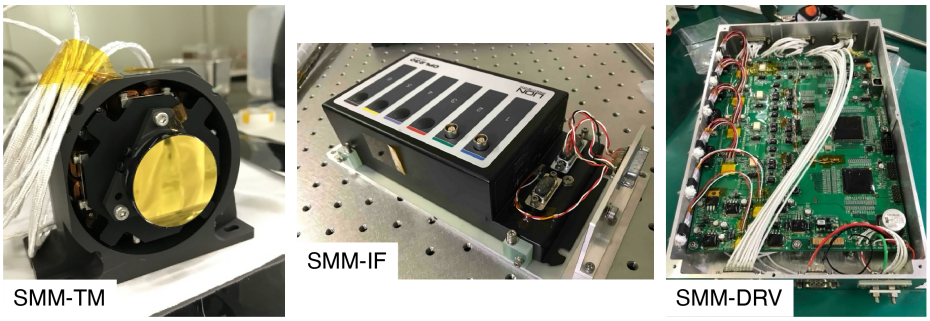


Figure 14. Tip-tilt mirror mechanism (SMM-TM) attached with the flight mirror with gold coating, electronics unit precisely reading gap-based capacitance sensors (SMM-IF), and its driver electronics (SMM-DRV). Modified from Oba et al. (2022).

Table 4. Basic features of SMM

Mechanism	
Tilt sensor	Gap-based capacitance sensor (2 sensors)
Actuator	Electromagnetic actuator (4 actuators)
Control frequency	Closed-loop control with > 90 Hz
Step resolution	0.0936" sky angle (2.857" mechanical angle)
Scanning range	$\pm$32.9" sky angle ($\pm$1005" mechanical angle)
Stability (3σ)	0.033" sky angle (1.0" mechanical angle)
Linearity	$< 0.15\%$
Step speed	< 31.3 ms, nominal 20 ms
Mirror	
Material	fused silica
Diameter	ϕ35 mm
Clear aperture	ϕ25 mm
Shape	convex sphere, curvature radius 425.4 mm
Coating	protected Ag coating

O-unit but in the ISLiD optics because the SMM-TM uses a convex spherical mirror located at a pupil position in the Offner relay-optical system feeding and focusing a solar image onto the SCIP slit (Korpi-Lagg et al. 2025). The SMM-IF has to be located close to the SMM-TM. The SMM-DRV is mounted on the gondola E-rack as with the PMU-DRV.

In the SMM-TM, a mirror is mounted on a stage supported by two sets of two flexural pivots, allowing for a two-dimensional tilt. The scan motion is performed only in one direction perpendicular to the slit in a standard observation, but the other direction can be used for coalignment purposes between ISLiD and SCIP and with the other on-board instruments. To precisely control the tilt of the mirror, a closed-loop control is implemented, which requires feedback to measure the tilt angles. Gap-based capacitance sensors (CPL230, Lion Precision) are installed behind the mirror of the SMM-TM. The output of the sensors is

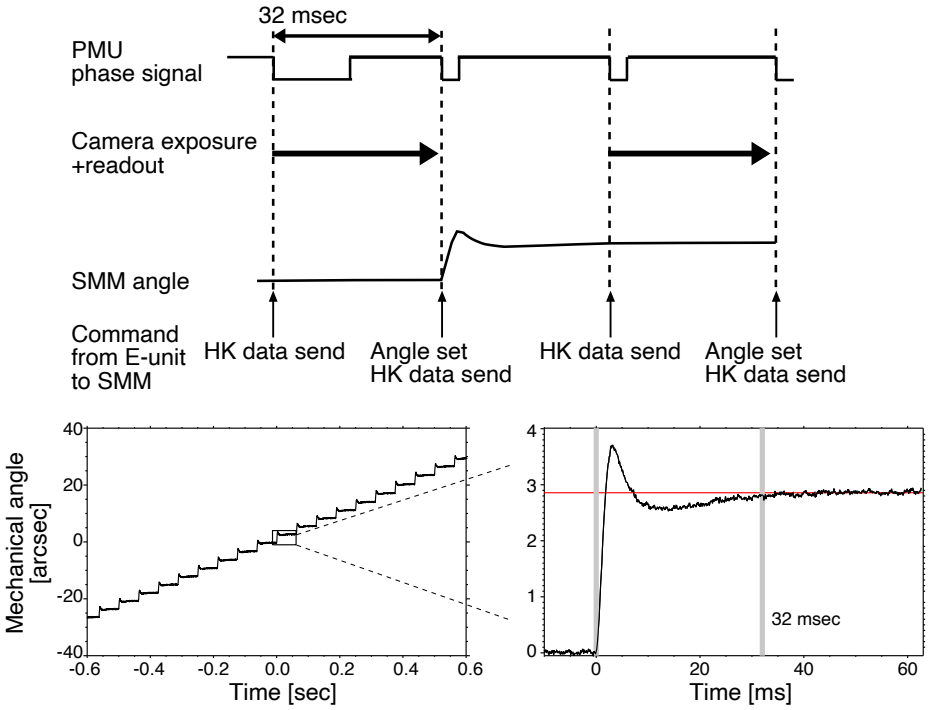


Figure 15. (top) Schematic illustration showing timing relationship among the PMU phase signals, camera exposures plus readouts, commands from the E-unit to SMM, and the SMM tilt angle. Note that this is the case for the fastest scan mode, where the camera exposure and readout are completed in 32 ms. (bottom) Test result of the scan motion in the fastest scan mode (64 ms step interval), measured by a position sensitive detector (PSD). A camera exposure starts from the gray line marked with 32 msec. Modified from Oba et al. (2022).

processed and immediately fed back to drive the electro-magnetic actuators with a control frequency larger than 90 Hz (crossover frequency).

Figure 15 (top) illustrates the time sequence among the SMM tilt angle, camera exposures plus readouts, and the PMU phase signals for the non-polarimetric, rapid mode (see Section 6.2 for details). As mentioned above, the SMM tilts the mirror toward the next position when receiving a tip-tilt command from the E-unit within 32 ms during non-exposure periods. The performance of the SMM was optically evaluated by installing a non-flight flat mirror of the same size and weight as the flight spherical mirror. The flat mirror allowed measuring tilt angles using an auto-collimator and a position sensitive detector (PSD). The optical measurements confirmed that the SMM fulfilled (1) the scan-step uniformity (linearity of 0.08%) across the wide scan range (±1005" in the mechanical angle), (2) high stability of 0.1" (3σ) in the mechanical angle, and (3) fast stepping speed shorter than 26 ms, as shown in Figure 15 (bottom). Details of the SMM test configuration and results are shown in Oba et al. (2022). After verification of the SMM performance, the non-flight flat mirror was replaced with the flight spherical one.

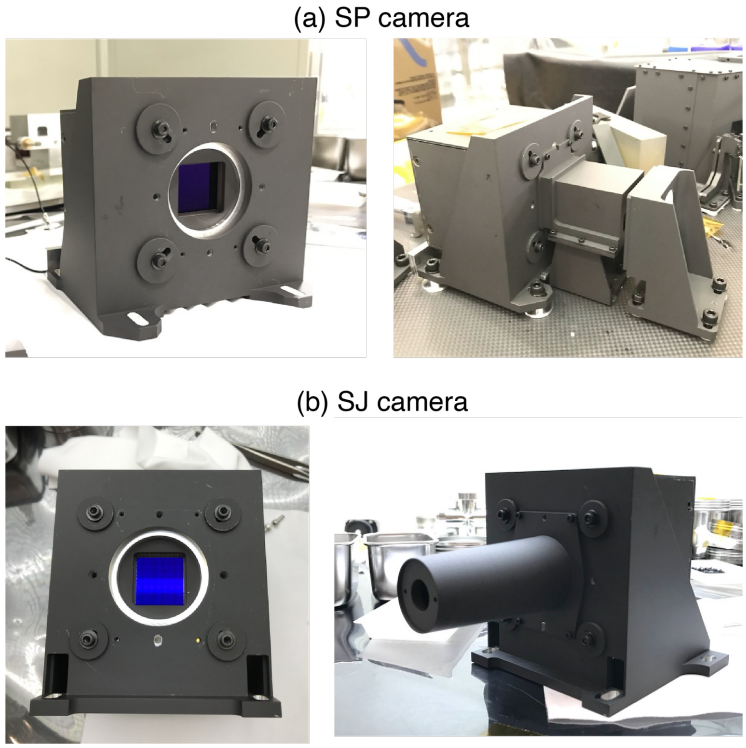


Figure 16. (a) One of the two SP cameras mounted on the camera bracket. A camera baffle structure was installed to enclose the optical path between PBS and the camera. (b) SJ camera mounted on the camera bracket. The SJ camera also has a camera baffle to suppress unwanted stray light.

3.5. Cameras

Specific, custom cameras were designed and manufactured for both the TuMag and SCIP instruments aboard SUNRISE III (Orozco Suárez et al. 2023), based on the back-thinned CMOS sensor GSENSE400BSI (Gpixel Inc.). In both instrument cameras, the detector has 2048×2048 pixels with an 11 μm pixel size, which, in the case of SCIP SP, images the $\sim$ 8.5 nm (CH1) and $\sim$ 7.5 nm (CH2) wide spectrum of a one-dimensional, 58″-long region of the Sun with 0.0935”/pixel spatial sampling for both orthogonal polarization states. The SJ camera has a wider FoV coverage than 60″×60″. The exposure time is adjustable up to 32 ms and depends on the SCIP observing modes (Section 6.2). The quantum efficiency of the sensor is as high as 60% and 40% at 770 nm and 850 nm, respectively. The sensor works in the rolling shutter configuration. The rolling shutter direction is selected to achieve a synchronous exposure in orthogonal polarization states at a specific wavelength in the SP observation, while an exposure is not exactly simultaneous in the wavelength direction. The scientific and system-engineering requirements for the SCIP cameras are summarized in Table 5. Figure 16 shows pictures of the SP and SJ cameras. The SP and SJ

Table 5. Main camera scientific and system-engineering requirements

Name	Symbol	Value	Units (Type)[a]
Sensor's quantum efficiency	Q	≥ 0.8 (peak in the visible light) ≥ 0.4 (SCIP wavelength ranges)	
Pixel full well		$\geq 6 \cdot 10^4$	e^-
Photon flux budget	F	$\geq 3 \cdot 10^4$	e^-
Photon response non-uniformity	f_{prnu}	$< 0.01\,F$	
Digital depth		12	bit
Pixel area		11×11	μm^2
Effective collecting area		2048×2048	pixels
Configurable readout speed		≤ 48	frames s^{-1}
Readout noise	N_{r}	< 10	e^-
Fixed pattern noise[b]	$N_{\mathrm{dc,fpn}}$	< 100	e^-
Dark current noise at 20°C	N_{dc}	< 50	e^-
Maximum camera envelope		$100 \times 80 \times 73$	mm^3
Optical entrance window		No	
Housing material		PCO black	
Thermal interface		Yes	Cold finger
CoaXPress coaxial connector		Yes	DIN 1.0/2.3 jack
Sensor's default operational temp.		20.0 ± 0.5	°C
Power consumption		< 6.9	W

[a]Units are per pixel where necessary.

[b]For the specified photon flux.

cameras have adopted horizontal and vertical rectangular shapes, respectively, as a result of a 90° rotation in the rolling shutter direction.

3.6. Thermal design

The thermal design of the SCIP units is driven by the Earth's stratospheric thermal environment, where Sunrise iii operates. For a flight altitude of 37 km, the air pressure is around 500 Pa, and rarefied gas heat transfer phenomena must be considered. The primary thermal interaction between the instrument and its environment is through radiation; therefore, a similar approach was followed to that taken towards the thermal design of low Earth orbit (LEO) satellites, and hot and cold cases were studied. However, in contrast to LEO satellites, a stratospheric balloon stays above the same region of Earth for a long period of time, and steady-state extreme case analyses can be used for dimensioning the thermal control subsystem. The hot and cold float cases are determined by the worst-case possible combination of the direct sunlight, albedo, Earth's outgoing longwave radiation (OLR), and the solar zenith angle (SZA). However, using the extreme values for the previously mentioned loads directly would lead

Table 6. Worst-case thermal environmental conditions for SCIP.

Parameter	Hot operational case	Cold operational case
Albedo	0.64	0.77
OLR (W/m^2)	237.5	176.5
SZA (°)	45.5	87.7

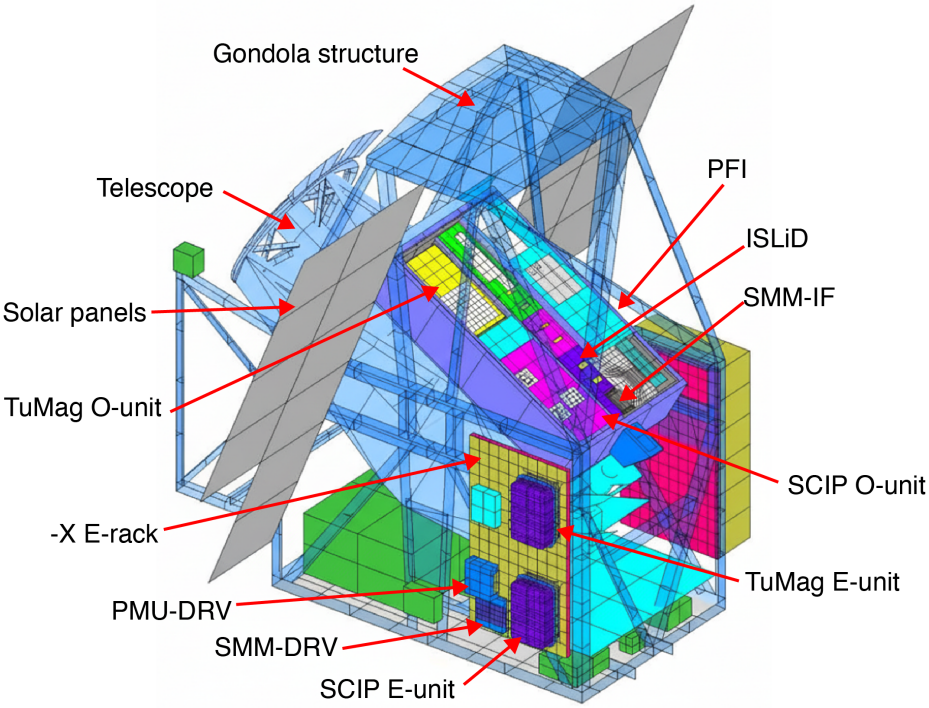


Figure 17. Geometrical Mathematical Model (GMM) for thermal analysis of SUNRISE III implemented in ESATAN-TMS, showing the mounting locations of the SCIP components. Modified from Piqueras et al. (2025).

to an oversized system, as the solar elevation angle, the albedo coefficient, and the OLR are partially correlated, and extreme values for all the loads do not occur at the same time. In the case of SUNRISE III, a new approach was followed to determine the albedo and OLR loads using measured data from NASA's Clouds and Earth Radiant Energy System (CERES) for the summer season and the region of interest (González-Llana et al. 2018). The obtained worst-case environmental conditions are summarized in Table 6.

During the ascent phase, due to the low temperatures and the relative air speed, it is possible to achieve the lowest temperatures. In the case of SUNRISE III, the SCIP O-unit is inside the PFI, protected against external winds by the so-called windshields. Additionally, the PFI receives direct sunlight that contributes to heating up the units because the gondola is allowed to spin during the first

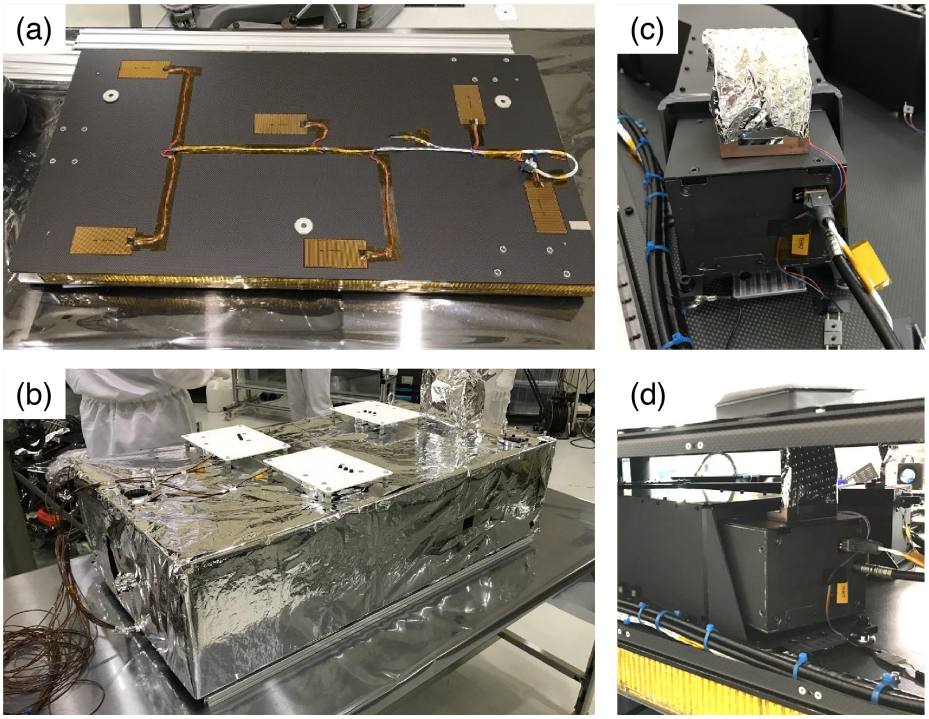


Figure 18. (a) Operational heaters attached on the bottom surface of the optical bench. (b) The SCIP O-unit covered by SLI in which the three radiators on the top face are connected to the two SP cameras and the SJ camera. (c) A flexible copper strap attached to the SP2 camera in which the strap is wrapped by SLI. (d) Connection of the SP2 camera and its radiator by the copper strap. Modified from Katsukawa et al. (2022).

phase of the ascent. After studying worst-case hot and cold launch scenarios, it was concluded that the float conditions shown in the previous paragraph and Table 6 were more extreme and therefore the ones used for sizing the thermal hardware (Fernández-Soler et al. 2021).

The SCIP O-unit is located in one of the corners of the PFI, as shown in Figure 17, along with the other units. All these units share a similar environment. However, the thermal requirements and operating conditions are different for each one, and so is their thermal design. The O-unit is intended to operate at near room temperature ($\sim 20^\circ$ C), but the PFI, in general, is colder. Therefore, in order to reduce heat losses to the PFI, and to decouple the behavior of the O-unit from the other PFI units and the PFI itself, the unit has been insulated conductively and radiatively. The O-unit is mechanically attached to the PFI by means of three titanium mounting points. These interfaces provide a high thermal resistance path, conductively decoupling the O-unit from the PFI. Additionally, to insulate radiatively, the O-unit is wrapped in single-layer insulation (SLI) made of aluminized polyimide films on both sides (Figure 18 [b]). We choose SLI over multi-layer insulation (MLI) because residual air makes gas conduction the dominant heat transfer mechanism, reducing the effectiveness of MLI and making the added complexity unnecessary.

Three cameras (SJ, SP1, and SP2) are located inside the O-unit. Each camera dissipates around 3.6 W during nominal operation, distributed as $\sim$ 0.6 W within the CMOS sensor and $\sim$ 3 W within the printed circuit board (PCB) with the control electronics (PCB–FPGA). The camera thermal requirements are the main drivers of the O-unit thermal design. The CMOS sensor of each camera needs to be maintained between 15 and 30°C with a temperature stability of $\pm$0.1°C. The CMOS sensor is in direct contact with a copper cold finger, which is mechanically attached to the top part of the camera. The top part of each of the cameras is refrigerated by three dedicated white-painted (Aeroglaze A276) radiators placed on top of the instrument (Figure 18 [b]). The camera and the radiators are connected by a flexible copper strap (TAI Corp. P5-503, Figure 18 [c][d]). A thermal filler (Gap Pad GPHC5.0) is inserted between the strap and the camera, as well as between the radiator and the strap to have good conductive coupling. The CMOS sensor operating temperature and thermal stability are achieved by a dedicated heater located on the cold finger and capable of dissipating up to 6 W.

The top part of the unit has direct view to the cold sky, but is also subjected to solar, albedo, and OLR loads. The camera radiators have been sized to maintain the CMOS sensor at 15°C for the worst hot operating conditions, so after adding temperature uncertainties, there is enough margin for the heater to stabilize the sensor below 30°C. The top part of the instrument, not used as the radiators, is insulated with expanded polystyrene (EPS) foam, wrapped in aluminized Mylar with the Mylar facing outside. Although this outer finishing does not provide the best radiative insulation, it was decided to use it to avoid overheating the top part during the ascent phase, when the telescope is fixed in horizontal position and there is direct sunlight, or in case of malfunction with the telescope pointing during float operation. In order to control the temperature of the rest of the components of the O-unit, operational heaters are placed on the optical bench. The heaters are controlled by the E-unit and have a maximum dissipation of approximately 25 W. Figure 18 (a) shows the operational heaters (6 pieces of Minco HK6913) attached to the bottom surface of the optical bench. For the ascent phase, and in case the E-unit is turned off, there are also non-operational heaters to maintain the optical bench above 0°C, in which Minco HK5171 together with CT198 are used for thermostat control.

The analysis and thermal design of the O-unit was performed with the help of an ESATAN-TMS, a widely used software package supported by the European Space Agency for conducting in-orbit thermal analysis based on the lumped parameter method, with a model including approximately 1000 nodes. The model implements all the main elements of the O-unit, as shown in Figure 19, and is integrated into the complete SUNRISE III thermal model shown in Figure 17. The SUNRISE III thermal model contains detailed models of most of the instruments, but due to its complexity, each analysis can last for several hours. In order to speed up calculations for the different units, equivalent boundary conditions are calculated for each one using the SUNRISE III thermal model. Then, an equivalent standalone analysis can be carried out independently for each unit. After a major update in the unit's model, the unit is integrated again in the SUNRISE III model, and new boundary conditions are calculated. Details on the thermal analysis of the SCIP O-unit are described in Piqueras et al. (2025).

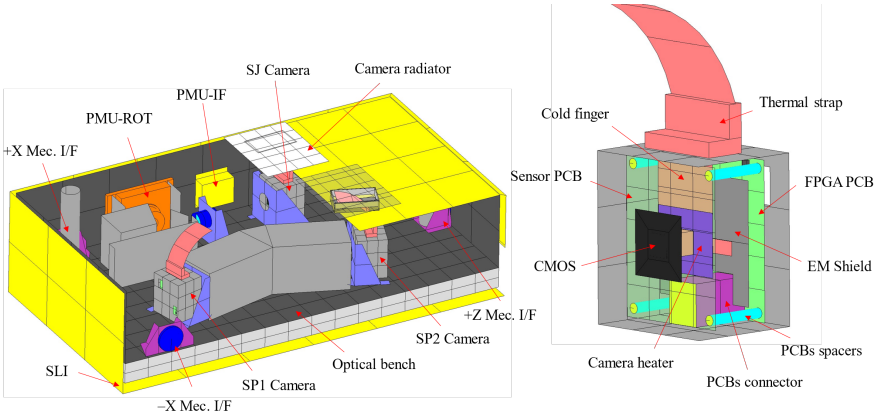


Figure 19. ESATAN-TMS GMM of the SCIP O-unit (left) and one of its cameras (right). Reproduced with permission from Piqueras et al. (2025).

4. SCIP E-unit

The SCIP E-unit houses electronic components on three specifically tailored PCBs: (1) the digital processing unit (DPU), (2) the analog, mechanisms, and heaters driver board (AMHD) and (3) the power converter module (PCM), as shown in the block diagram (Figure 5). To meet the harsh environment of a stratospheric flight, along with the limited budget compared to space missions, we designed the E-unit based on commercial-off-the-shelf (COTS) components. Consequently, the electronic components and boards of the E-unit have to be enclosed in a pressurized vessel under temperature control, so that we can use commercial devices without any concern about their near-vacuum behavior. The development time is another important factor to take into account: the use of general-purpose, modern components —not qualified for space, together with state-of-the-art software tools, sharply reduces the engineering efforts. A further driver of this development was the maximization of commonalities between the electronics units of TuMag and SCIP, which were developed by the same group at the same time. The same three PCBs are used in TuMag, whereas a fourth board used in TuMag, the high-voltage power supply board, is not needed for SCIP. The electrical harness connections between the SCIP components are summarized in Appendix A.4.

4.1. The electronic boards inside the E-unit

4.1.1. The DPU board

The DPU board includes two main blocks: a system controller (SyC) and a frame grabber (FG), which also acts as an image processor, as shown in Figure 20. The SyC performs tasks such as image storage management, housekeeping data acquisition, instrument state monitoring, and communications with the balloon platform and the ground support software. The FG has to guarantee

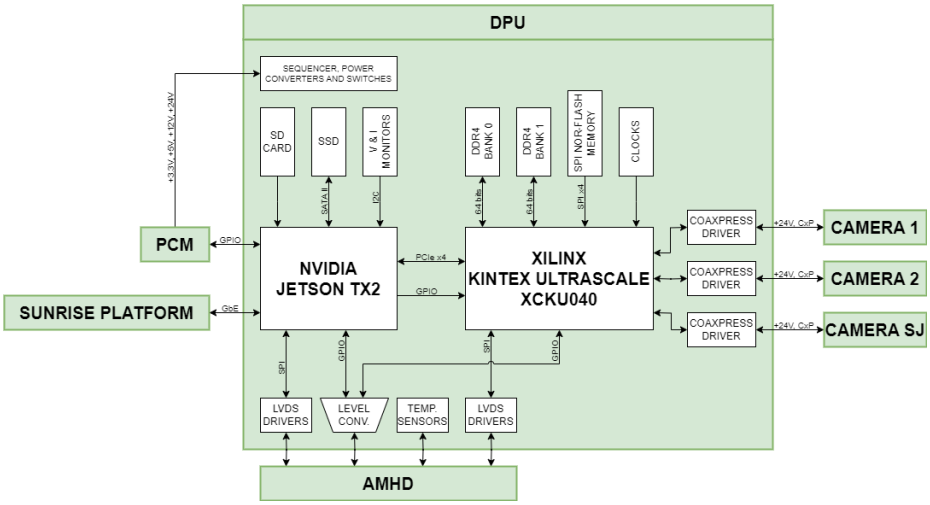


Figure 20. Functional block diagram of the DPU board. The central blocks represent the system controller (SyC; NVIDIA^{TM} Jetson TX2) and the frame grabber (FG; Xilinx^{TM} Kintex Ultraescale).

synchronization between subsystems and to perform intensive image processing tasks such as acquisition, polarization demodulation, accumulation, and bit compression of the images (Appendix A). Both devices are the same as those used in TuMag, and their detailed description can be found in Section 6.1 of del Toro Iniesta et al. (2025).

One difference from the TuMag's DPU is that the FG's Field Programmable Gate Array (FPGA) carries out the image acquisition and processing from the three scientific cameras (SP1, SP2, and SJ), instead of two cameras in the TuMag case. The processing pipeline for SP1 and SP2 is nearly identical and includes image demodulation-accumulation, bit-compression, and standard image compression. By contrast, the SJ camera is processed in the SP1's pipeline using a time-multiplexed scheme. In order to keep synchronization with the PMU phase, the timing of the camera triggers and the SMM commanding are controlled by the FG. For this purpose, it includes a custom core called SCIP Control Unit, which decodes the PMU phase signal and generates the sequence of CoaXPress (CxP) camera triggers and SMM-movement interrupt signals. The latter signals are received by the Microblaze processor, which executes a specific interrupt routine to command the SMM by the serial peripheral interface (SPI). These SPI commands are eventually interpreted by the AMHD board, which implements the physical interface with the SMM-DRV.

4.1.2. The AMHD board

The AMHD interfaces the O-unit as well as the DPU and PCM boards in the E-unit to acquire the instrument status telemetry, drive the mechanisms, and stabilize the instrument temperatures by controlling the heaters. An AMHD functional diagram is shown in Figure 21. The blocks of the housekeeping (HK)

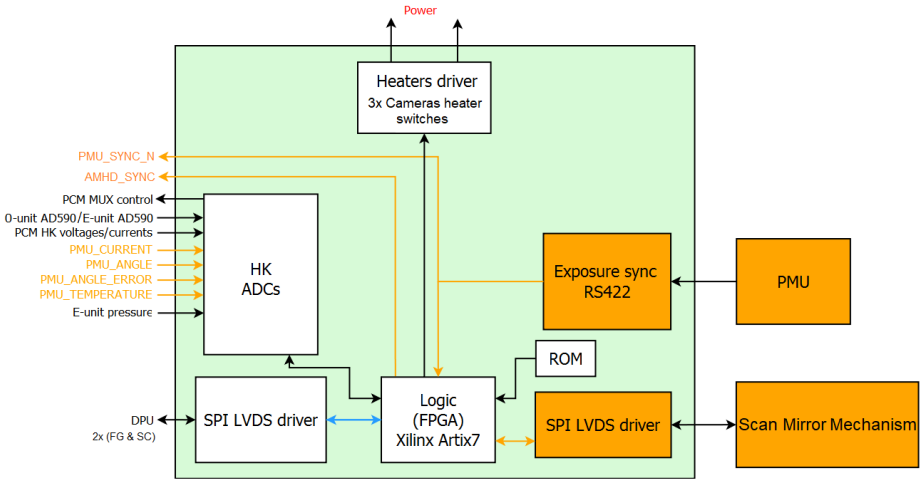


Figure 21. Functional block diagram of the AMHD board.

analog-to-digital converters (ADCs), the driver controlling the interfaces with the DPU, the heater driver, the logic "brain" of the board, and a read-only memory (ROM) are the same as those in the TuMag AMHD (see Section 6.2 in del Toro Iniesta et al. 2025). The following blocks are specific to SCIP:

i) An RS-422 receiver to obtain the PMU synchronization signal. This logic has two main features. First, it routes the PMU synchronization signal to the FG. Second, it ensures signal integrity at the FG even if communication with the PMU is lost.
ii) A dedicated SPI with the SMM to control it and acquire its HK data. The frequency for regular HK is configurable, but the PMU and SMM subsystems' HK is acquired every 32 ms at the configured frequency.

4.1.3. The PCM board

The PCM is the electronic subsystem that powers the SCIP E-unit and provides it with the required voltages. Five secondary output lines of the PCM and their approximate maximum average power consumption in the so-called operational mode of the instrument are summarized in Table 7. In addition, an unregulated $\sim$ +25.6 V (average of $V_{\rm in}$) output is also delivered from the PCM primary side, after a common-mode filter and an inrush-current limiter circuit, through the AMHD board. The design of the PCM is almost the same as that in TuMag (Section 6.4 in del Toro Iniesta et al. 2025). One difference from the TuMag PCM is that the number of dedicated COTS +24 V DC/DC converters is reduced from two to one because the high-voltage power-supply board is not needed for SCIP. Another difference is that the unregulated power ($V_{\rm in}$) is delivered to the PMU and SMM, as well as the various heaters in the instrument.

Table 7. SCIP operational-mode maximum average power of each output.

Voltage	Power	Subsystem
+3.3 V	5.0 W	DPU, AMHD
+5.0 V	4.0 W	DPU, AMHD
+12.0 V	36.0 W	DPU, AMHD, Mechanisms
−12.0 V	0.5 W	AMHD
+24.0 V	10.0 W	Cameras
V_{in}	45.0 W	Heaters
	31.0 W	PMU, SMM
Total approx.	131.5 W	

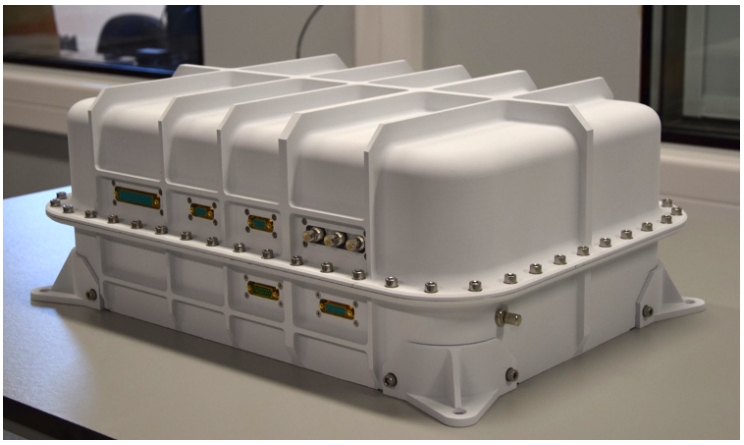


Figure 22. Enclosure box of the SCIP E-unit. Connectors can be distinguished.

4.2. The pressurized electronics box

The pressurized enclosure of the SCIP E-unit (Figure 22) houses the three electronic boards (PCM, DPU, and AMHD) in charge of the necessary functions for the instrument. The use of COTS electronic components, instead of military- or space-grade ones, is enabled by a pressurized box capable of maintaining an internal pressure slightly above 1 atm to guarantee the proper functioning of the circuits. The box is filled with dry nitrogen, preventing water condensation at low temperatures. As with TuMag, a "book-like" design has been devised so that the box is opened in two halves during Assembly, Integration, and Verification (AIV) stages in order to ease the assembly and verification of the electronic components and their interconnections. Once all the components are attached, the two halves are closed and screwed together through a flange with an O-ring seal to prevent pressure losses. Stiffeners are included in the design to guarantee the required rigidity of the structure while maintaining a low wall thickness to reduce mass. The box envelope is 584 mm × 404 mm × 226 mm. It hosts electrical connectors and provides the interface attachments with the SUNRISE III electronic rack.

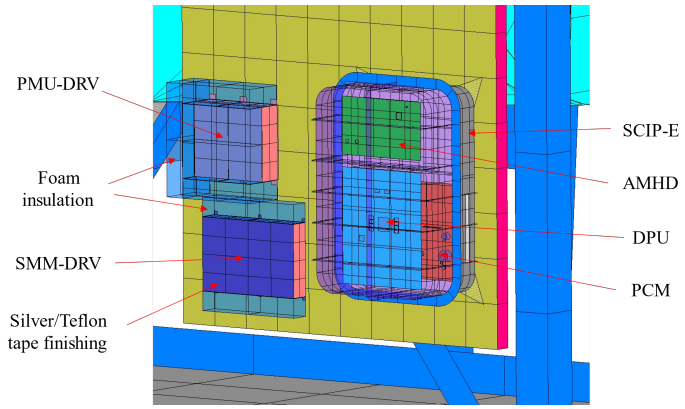


Figure 23. ESATAN-TMS GMM of the SCIP E-unit, PMU-DRV, and SMM-DRV mounted on the E-rack. Reproduced with permission from Piqueras et al. (2025).

Connectors are also included for data transmission and for power supplies. The box surfaces are treated with a chromium-process coating in order to obtain good thermal and electrical conductivity. The outer ones are white painted (using SG121-FD from MAP company) for radiative cooling.

4.3. Thermal design

The SCIP E-unit, PMU-DRV, and SMM-DRV are mounted on one of the E-racks of Sunrise iii (Figure 17). The E-racks are shielded from external winds by transparent windshields allowing solar and infrared radiation to pass through. The thermal-design concept for the SCIP E-unit is identical to that of the TuMag E-unit because the two E-units are located on the same E-rack and experience the same thermal environment (see del Toro Iniesta et al. 2025, for details). Thermal models for the E-unit, together with PMU-DRV and SMM-DRV, was developed using ESATAN-TMS. While the stratospheric thermal environment resembles the space environment in terms of heat transfer and environmental loads, certain situations still require consideration of convection interactions. Because the E-unit is pressurized, additional couplings among electronic components, the housing, and the nitrogen inside have been accounted for. A simplified thermal model (Figure 23) is integrated into the complete Sunrise iii model to obtain thermal boundary conditions for each electronic unit. A detailed thermal model was then analyzed separately for each unit, following the methodology outlined in González-Bárcena et al. (2017). Detailed thermal analyses of the E-unit, PMU-DRV, and SMM-DRV are summarized in Piqueras et al. (2025).

5. On-board software, firmware, and data flow

The SCIP on-board software is divided into two main blocks: the control software (CSW) and the frame grabber software (FGSW). The CSW, which runs in the

SyC, is mainly devoted to telecommand (TC) and telemetry (TM) management,[1] transferring images from the FG to the SUNRISE ICS, generating thumbnails from selected images, housekeeping acquisition, and contingency management. The FGSW, which runs within the FG's MicroBlaze processor, commands the different subsystems during the observation modes, handles the commands from the SyC, and manages the image transfer from the FG to the SyC.

The basic design of the software (CSW and FGSW) and the data flow are identical to those of TuMag. A graphical user interface called GUISCIP runs on ground support equipment. It provides the same functionality as TuMag's interface but is customized for SCIP operations. Details of the software and the ground support equipment are described in Sections 8 and 9 of del Toro Iniesta et al. (2025), respectively. In contrast, the firmware implementation is tailored to the on-board processing required by the SCIP observing modes, and its details are provided in Appendix A.

6. Assembly and test of SCIP

6.1. Optical alignment

Because the SCIP O-unit does not have any adjustable mechanisms except the rotating waveplate and the scan mirror mechanism, careful optical alignment is necessary to achieve the spatial and spectral resolution described in Section 3.1. It is especially important to coalign positions and tilts of the collimator and camera mirrors as well as the tilt of the echelle grating with respect to the slit in the spectrograph (Kawabata et al. 2022a). These optical elements were first installed on the optical bench, and their rear and side surfaces were measured using a coordinate measuring machine (CMM, Mitsutoyo LEGEX 910) as shown in Figure 24 (a). These elements were mechanically aligned by fabricating the adapter plates (Figure 10 [a]), which were inserted between the optical bench and the mirror support mechanism.

After the mechanical alignment, the optical elements were finely coaligned by shimming based on optical measurements. A telecentric feed optical system was constructed to feed the F/24.2 beam, same as ISLiD, into the O-unit (Figure 24 [c]). The coalignment measurement was done by feeding light from tunable lasers for 850 nm and 770 nm bands (Sacher Lasertechnik TEC-520). A non-flight CMOS camera (ASI1600MMPro) was mounted on the camera bracket for the optical alignment test because it had a smaller pixel size of 3.8 μm than the flight camera (Figure 24[b]).

We measured the astigmatism aberration by manually defocusing the camera (Figure 24[d]) and subsequently co-aligned the collimator and camera mirrors to minimize astigmatism aberration. After the coalignment of the mirrors, we mounted the flight camera and made a focus scan to find the best focus position.

[1] Telecommands are orders to the instrument through the SUNRISE III instrument control system (ICS). Telemetries are data transferred from SCIP to the ICS.

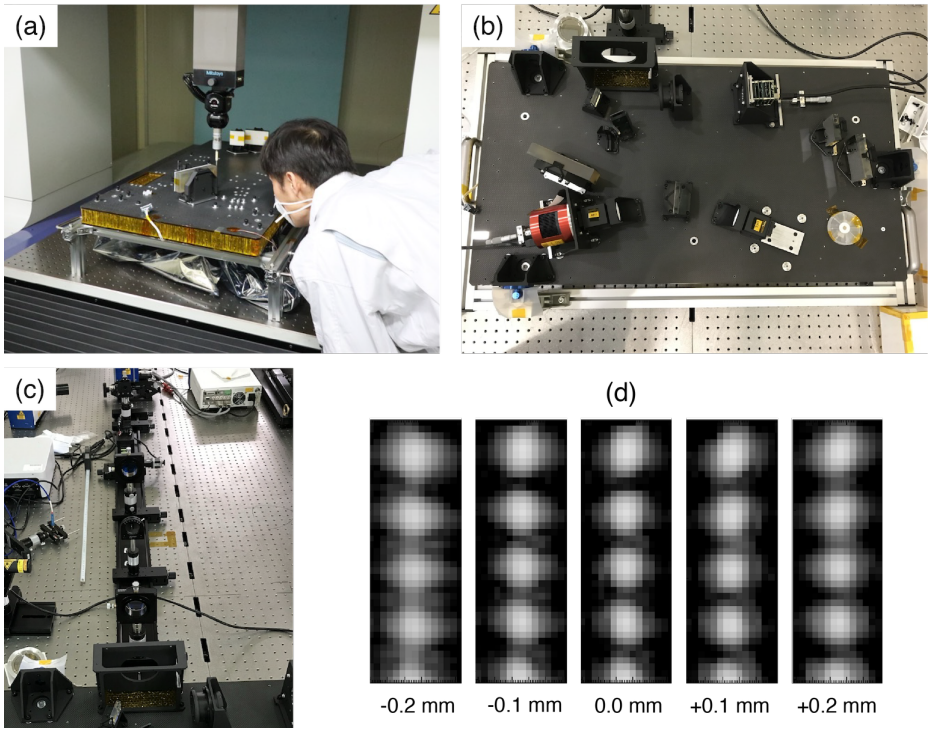


Figure 24. (a) Mechanical alignment measurement with CMM for the SCIP spectrograph optical components. (b) The SCIP O-unit configured for the optical alignment measurement using a non-flight camera mounted on the camera bracket. (c) Feed optical system for the optical alignment measurement. (d) An example of a focus scan result measured with the non-flight camera. Modified from Kawabata et al. (2022a).

We evaluated the spatial Modulation Transfer Function (MTF) of the spectrograph by feeding light from a white light lamp (NIHON PI PIS-UHX-NIR) through Ronchi ruling targets of 20, 30, and 40 lines/mm which were arranged perpendicular to the slit direction in the feed optical system. We demonstrated that the spectrograph met the wavefront error required by the optical design (Figure 25).

The spectrum and spatial positions measured on the SP cameras were verified by feeding natural sunlight to measure the solar spectral lines using a heliostat implemented at the NAOJ Advanced Technology Center (ATC) cleanroom facility, as shown in Figure 26.

The SJ optical system is less sensitive to the coalignment, but we checked the tilt of the SJ reflective filter and the SJ lens unit by measuring a star target image created by the feed optical system. The focus position of the SJ camera was adjusted by looking at the sharpness of the slit. Because the SJ optics use a lens system that causes a non-negligible focus offset of 0.33 mm between air and vacuum, the offset was applied in the SJ camera position after finding the best position in air. The focus offset was verified in the thermal vacuum test described in Section 6.4.1.

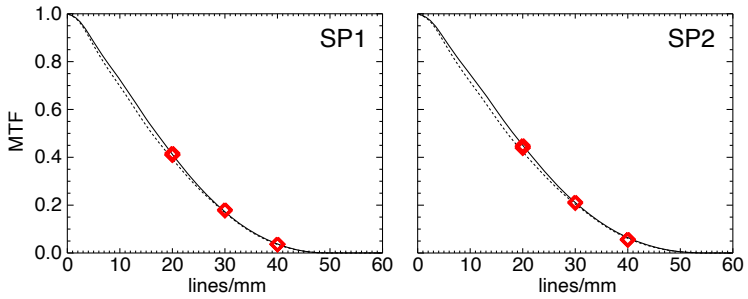


Figure 25. MTF of SP1 (left) and SP2 (right). The solid and dashed lines show an ideal MTF with no wavefront error (WFE) and an MTF with WFE of 40 nm rms, respectively. The red diamonds represent the Ronchi ruling measurements at 20, 30, and 40 lines/mm. Modified from Kawabata et al. (2022a).

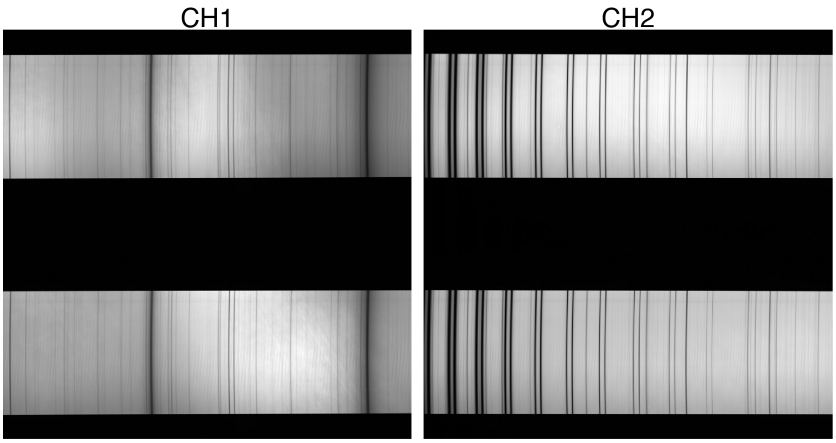


Figure 26. SP1 (left) and SP2 (right) data taken by feeding the natural sunlight. The horizontal and vertical directions correspond to the wavelength and spatial directions, respectively. The s- and p-polarization spectra are vertically separated by the PBS (Figure 7) and focused onto the same sensor. Modified from Kawabata et al. (2022a).

6.2. Synchronization test

The SCIP observation requires synchronous control among the rotating phases of PMU, the scan motion of SMM, and the exposures by the three cameras. The SCIP E-unit manages synchronization control of the components according to the phase signal sent from the PMU. Figure 27 shows the timing diagram of the PMU phase signal, camera exposures and their readout for the SP and SJ cameras, and SMM angle set commands and associated motions. The length of the pulse in the PMU phase signal represents the rotation phase of the waveplate: the longest, mid-long, and nominal pulses arrive every 360°, 90°, and 22.5°, respectively. The SP cameras start an exposure of the first column in its sensor at the leading edge of the pulses and then send images to the demodulation buffer in the DPU. The exposure start times of the first and last columns differ by 21 ms because of the rolling shutter of the sensor. To avoid mirror motion

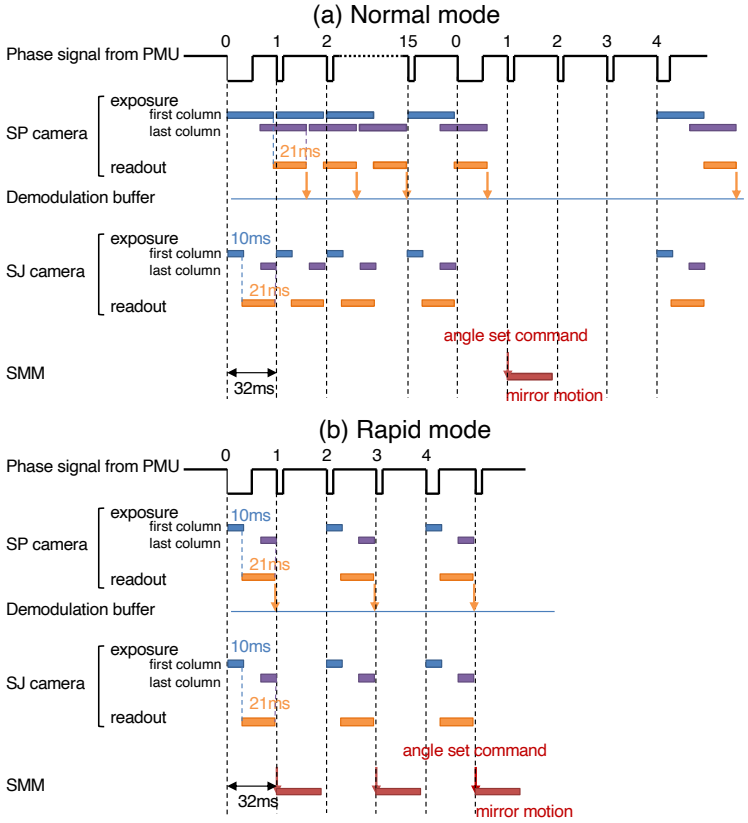


Figure 27. Timing diagram of the PMU phase signal, camera exposures and readouts by the SP and SJ cameras, onboard demodulation, and SMM angle set commands and associated scan motion in the (a) normal and (b) rapid modes. Modified from Kubo et al. (2023).

during exposure, the angle set command is sent to the SMM after the exposure of the last column is completed in both normal and rapid modes. In the normal mode, SP images sent to the DPU are demodulated and accumulated to produce a set of images corresponding to Stokes I_d, Q_d, U_d, V_d, and R_d parameters (Appendix A.2), while SJ images are transferred without onboard processing. Note that I_d, Q_d, U_d, V_d, and R_d are results of the demodulation operation and therefore differ from the true Stokes parameters. In particular, the new parameter R_d is used to introduce a 45°phase shift with respect to Stokes V and to compensate for the rolling shutter effect of the SP cameras (Kawabata et al. 2022b). In the rapid mode, both SP and SJ cameras obtain eight images per one PMU rotation, i.e., every 64 ms, and no onboard image processing is applied in the DPU.

After the component-level testing, the PMU, SMM, cameras, and E-unit were integrated to demonstrate the synchronization performance with the required accuracy. The timing relationship between image acquisition by the camera and the SMM mirror motion was investigated by Oba et al. (2022), who demonstrated that the scan mirror motion and an exposure did not overlap with the

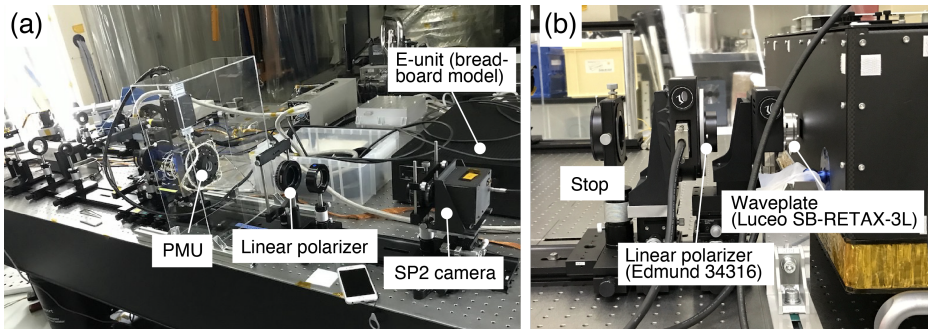


Figure 28. (a) Test configuration to verify the synchronization between the PMU and the SP camera. (b) Configuration of the instrument-level polarization calibration, in which a linear polarizer and an achromatic waveplate are located in front of the O-unit optical entrance. Modified from Kawabata et al. (2022b).

10 msec exposure duration used in the rapid mode observation. To verify the synchronization between the PMU and the SP cameras before installing them into the O-unit, using a similar configuration as used for measuring the rotation angle errors (Section 3.3), we measured intensity modulation with one of the SP cameras and verified that the exposure timing was consistent with the design. After installing the PMU and cameras into the O-unit, the synchronization between the PMU and the SP cameras was finally verified by the instrument-level polarization calibration described in Section 6.3.

6.3. Polarization calibration

The onboard demodulation operation produces Stokes I_d, Q_d, U_d, and V_d (and R_d) data from images taken with the SP cameras using the fixed arithmetic scheme described in Appendix A.2. The incident Stokes parameters and the demodulation output can be related by a response matrix $\boldsymbol{X}_0$ in the following equation (Elmore 1990; Ichimoto et al. 2008),

$$\begin{pmatrix} I_d \\ Q_d \\ U_d \\ V_d \end{pmatrix} = \boldsymbol{X}_0 \begin{pmatrix} I \\ Q \\ U \\ V \end{pmatrix} \tag{1}$$

where $(I_d, Q_d, U_d, V_d)^{\mathrm{T}}$ is the output of the demodulation operation and $(I, Q, U, V)^{\mathrm{T}}$ is the incident Stokes vector. Because the CMOS sensors used in the SCIP cameras work in rolling shutter configuration, the exposure start time linearly varies along the rolling shutter direction, which causes polarization crosstalk between Q_d and U_d, and between V_d and R_d. They are easily corrected by applying a rotation matrix corresponding to the phase shift due to the rolling shutter to $(Q_d, U_d)^{\mathrm{T}}$ and $(V_d, R_d)^{\mathrm{T}}$, respectively, to obtain $(Q'_d, U'_d, V'_d)^{\mathrm{T}}$. Then the response matrix $\boldsymbol{X}$ is obtained to relate $(I_d, Q'_d, U'_d, V'_d)^{\mathrm{T}}$, demodulation output after the rolling shutter correction, with $(I, Q, U, V)^{\mathrm{T}}$, incident Stokes

vector, i.e.,

$$\begin{pmatrix} I_d \\ Q'_d \\ U'_d \\ V'_d \end{pmatrix} = \boldsymbol{X} \begin{pmatrix} I \\ Q \\ U \\ V \end{pmatrix}. \tag{2}$$

Extensive instrument-level polarization calibration was employed to get the response matrix $\boldsymbol{X}$ considering spatial and wavelength dependence for both SP channels and both s- and p-polarizations (Kawabata et al. 2022b). In the feed optics used in the optical alignment (Section 6.1), a wire-grid linear polarizer and an achromatic waveplate (Luceo SB-RETAX-3L) were inserted in front of the O-unit optical entrance (Figure 28 [b]). They were rotated to specific angles by motorized rotation stages to feed specific polarization states from the halogen lamp. In total, 68 sets were taken at different angles of the linear polarizer and the waveplate. Along with the elements of the response matrix at each pixel, the origin of the waveplate angle and the waveplate retardation were simultaneously derived by a least-squares fitting.

Because SCIP is designed to have the polarization modulator at the optical entrance and to minimize internal instrumental polarization crosstalk, the response matrix is expected to be close to an ideal one. When the retardation of the rotating waveplate is 125°, the ideal response matrix of SCIP is given as

$$\boldsymbol{X}_{idel} = \begin{pmatrix} 1 & 0.213 & 0 & 0 \\ 0 & 0.502 & 0 & 0 \\ 0 & 0 & 0.502 & 0 \\ 0 & 0 & 0 & 0.502 \end{pmatrix}.$$

The measured response matrices, averaged over spatial and wavelength directions, yielded

$$\boldsymbol{X}_{ch1} = \begin{pmatrix} 1.000 & 0.207 & 0.003 & -0.001 \\ 0.000 & 0.500 & 0.049 & 0.000 \\ 0.000 & -0.049 & 0.500 & 0.000 \\ 0.000 & -0.001 & 0.000 & 0.435 \end{pmatrix}$$

$$\boldsymbol{X}_{ch2} = \begin{pmatrix} 1.000 & 0.208 & -0.002 & -0.004 \\ 0.000 & 0.497 & 0.054 & 0.000 \\ 0.000 & -0.054 & 0.497 & 0.000 \\ 0.000 & -0.004 & 0.000 & 0.434 \end{pmatrix}$$

for each channel. Detailed results of the instrument-level polarization calibration including the stability of the above response matrices against temperature variations are summarized in Kawabata et al. (2022b).

After SCIP was mounted into the PFI and the telescope, the polarization response matrices were updated by the polarization calibration measurements from the primary focus (F1), accounting for the polarization effect of the telescope except for the primary mirror. We mounted the same achromatic wave plate and a Glan-Taylor linear polarizer at F1 and produced various polarization states from a LED lamp, which were specific for the SCIP wavelength range. The

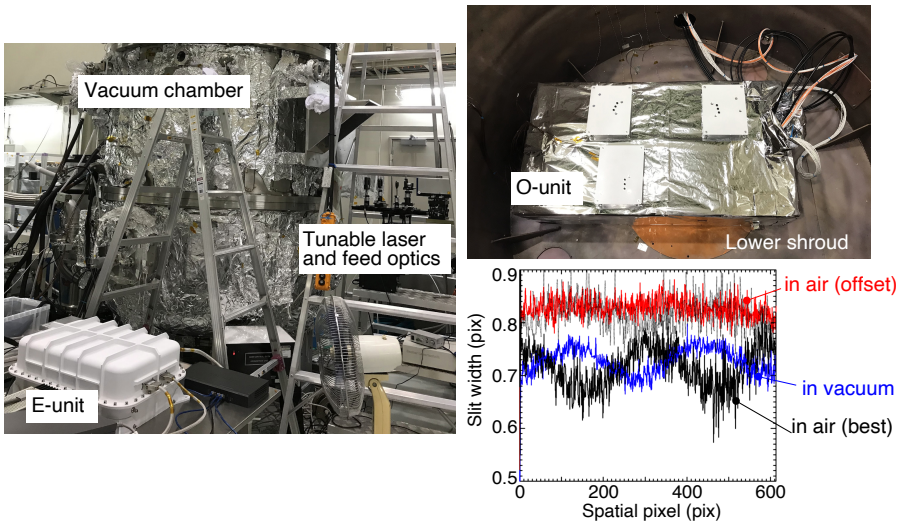


Figure 29. Outlook of the vacuum chamber for the O-unit TVT (left) showing the layout of the feed optics for the optical test and the SCIP E-unit. The SCIP O-unit was positioned on the lower shroud of the vacuum chamber (top right). The slit width measured with SJ in the TVT (bottom right) shows the best focus in air (black), offset position in air (red), and offset position in vacuum (blue). Modified from Katsukawa et al. (2022).

response matrices by the F1 polarization calibration are used to calibrate the flight polarization data.

6.4. Thermal-vacuum tests

6.4.1. O-unit TV test

The SCIP O-unit was subjected to a thermal-vacuum test (TVT) in which the O-unit was installed in a vacuum chamber and was exposed to the thermal vacuum environment expected during the balloon flight. The test was aimed (1) to correlate predictions from the O-unit thermal model with the measured temperature distribution in the O-unit (Section 3.6) and (2) to verify the expected spatial and spectral resolutions in the thermal vacuum environment. The TVT was carried out using a vacuum chamber at NAOJ ATC. As shown in Figure 29 (top right), the SCIP O-unit was placed in the lower shroud of the chamber, which simulated the PFI environment, with insulation by glass-epoxy spacers, while the upper shroud, not shown in the picture, simulated the radiator environment by maintaining a lower temperature than the lower shroud. The E-unit was located outside the vacuum chamber and was connected to the O-unit through a vacuum feedthrough in this TVT (Figure 29 left). This is because the E-unit was tested in a separate TVT in Spain to simulate the different thermal environments between the O-unit and the E-unit (Section 6.4.2). The detailed test configuration is shown in Katsukawa et al. (2022). Correlating the thermal model predictions with the temperature distribution measured through

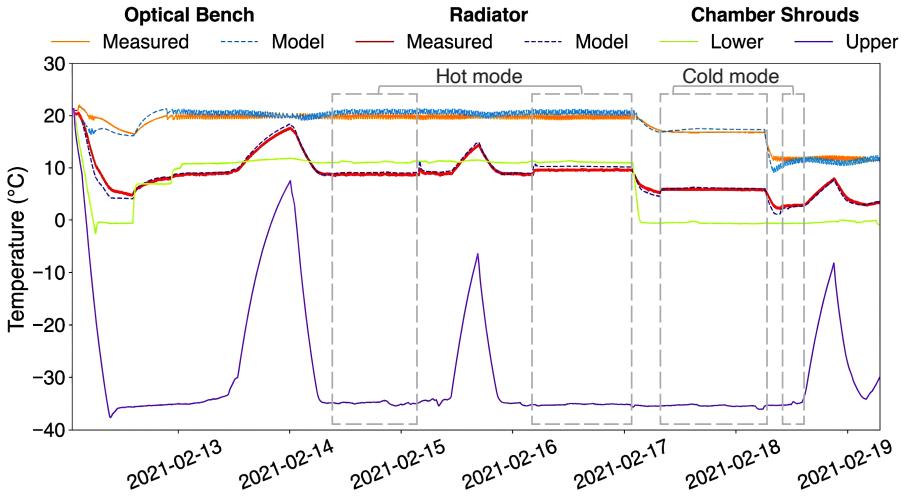


Figure 30. Temperature plots of the O-unit TVT. The orange and red lines show measured temperatures of the optical bench and camera radiator, respectively. The light-blue and blue dashed lines show their model temperatures. The light-green and purple lines show the chamber shroud temperatures. The gray dashed boxes indicate the period during which the measured and model temperatures were correlated in the hot and cold modes. Modified from Katsukawa et al. (2022).

the TVT was especially important for verifying the thermal design, because the flight conditions could not be reproduced completely on ground. Therefore, the in-flight behavior needed to be predicted by the thermal model. The agreement between the thermal model and the measured data is also shown for the optical bench (orange and light-blue lines) and the camera radiator (red and blue lines) in Figure 30 during some phases of the TVT. Detailed model correlation results are provided in Piqueras et al. (2025).

Because some of the optical properties in the O-unit were designed to behave differently in air and in vacuum, we constructed the test configuration to verify those properties by injecting laser and white light through a vacuum window (Figure 29 left). The air-to-vacuum shift of spectral positions was measured by feeding tunable laser light into the spectrograph for both the 850 nm and 770 nm bands. Spectral profiles of the laser verified the spectral resolution in different temperature conditions. We found that the spatial position of the spectrum data varied associated with the temperature ripple caused by switching the heater ON/OFF of the optical bench. This was caused by a slant of the collimator and camera mirrors, and the grating, due to a bi-metallic effect in their support mechanisms (Uraguchi et al. 2023). The temporal variation of spatial and spectral positions of the spectrum data could be corrected by post-processing during the flight. The air-to-vacuum focus shift of the SJ was verified by measuring the width of a slit image illuminated with white-light. In air, the SJ camera focus was shifted by a known amount of 0.33 mm from the best position determined by the narrowest slit width in a focus scan (Section 6.1). In the TVT we confirmed

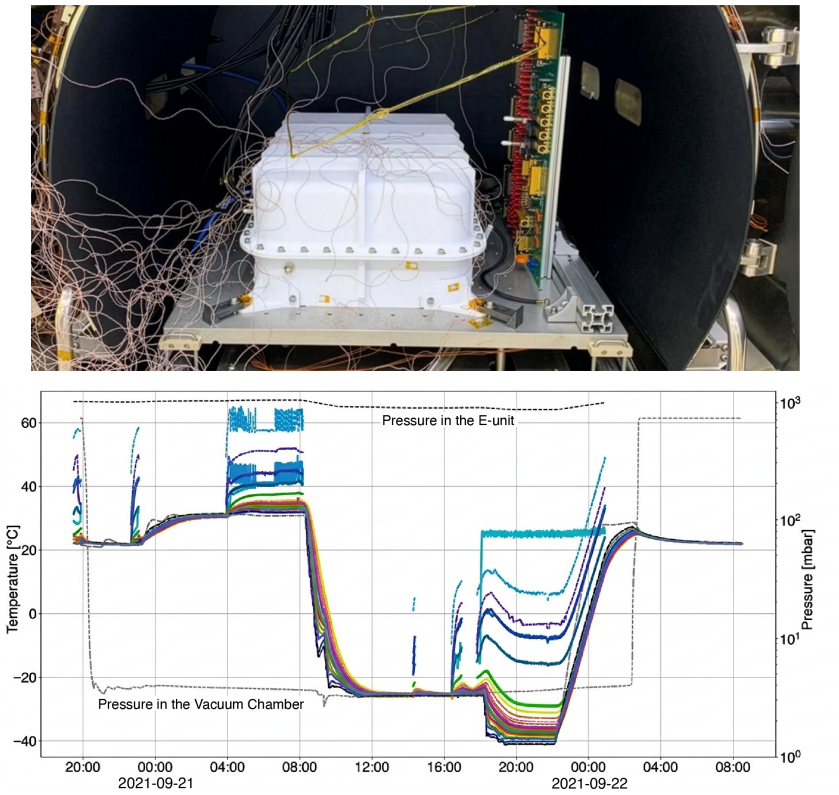


Figure 31. SCIP E-unit during the TVT with the electrical ground support equipment on the right (top). TVT temperatures and pressure plot (bottom). The dashed lines show pressures inside the vacuum chamber and the E-unit, while the other solid lines show temperatures of components in the E-unit.

that the slit width measured by the SJ recovered the narrowest width at the best focus position in air (Figure 29 bottom right).

6.4.2. E-unit TV test

The E-unit was tested under low vacuum conditions at IDR/UPM facilities (see Figure 31). Testing was conducted in a nitrogen atmosphere at flight pressure to verify proper operation and to ensure that no leakage occurred. Because reproducing the precise stratospheric environment was not feasible, the chamber's conductive and radiative interfaces were configured to achieve the worst calculated temperatures at the unit reference point with qualification margins of ±15°C. The design process was completed by correlating the detailed model of the E-unit (Section 4.3) with the test data. After this correlation, the model predictions showed a maximum discrepancy of less than 3°C compared with the test data.

7. Summary

SCIP is a new spectropolarimeter instrument that was developed for the third flight of the Sunrise balloon-borne solar telescope. It simultaneously measures full Stokes profiles of multiple spectral lines in near-infrared wavelength ranges around 770 nm and 850 nm. The wavelength ranges include photospheric Fe I 846.8 nm, upper photospheric K I 766.5 nm and 769.9 nm, and Ca II 849.8 nm and 854.2 nm, which provides good sensitivity to the Zeeman effect so that we can measure magnetic fields from the photosphere to the chromosphere. Owing to the 1 m aperture telescope and the greatly reduced influence of atmospheric seeing at the balloon altitude, SCIP can measure these spectral lines with good spatial and spectral resolutions of 0.21" and 1×10^5, respectively, enabled by corresponding samplings of 0.094" and 2×10^5. Considering the telescope and instrument throughput, the instrument achieves a polarization sensitivity of 0.03% (1σ) with a 10 sec integration time and 2 pixel binning along the slit in the 850 nm band, whereas no binning is needed in the 770 nm band. The SCIP O-unit is designed to achieve these performances by a combination of spectrograph and slit jaw optics, opto-mechanics and thermal control, the PMU utilizing the rotating waveplate, and the SMM for scanning the FoV. The E-unit is designed to control synchronization among the PMU, SMM, and cameras, process the acquired data, output it to the ICS, and perform housekeeping for the entire SCIP system. After verifying the performance of SCIP through ground testing, it was integrated into the Sunrise III PFI and the telescope. During the flight of Sunrise III in July 2024, SCIP successfully operated and obtained spectropolarimetric data for various solar targets, including the quiet Sun, sunspots, plages, etc. By combining the data from SUSI and TuMag, which are also onboard Sunrise III, SCIP is expected to provide unique data to understand energy transfer and dynamical processes taking place through the photosphere–chromosphere.

Acknowledgements We would thank the significant technical support given by the Advanced Technology Center (ATC), NAOJ. Engineering support from Mitsubishi Precision Co., Technocraft, Mitsubishi Electric Co., and Syouei System Co. is gratefully acknowledged for the development of the PMU and SMM mechanisms. High-precision optics mounted on the SCIP O-unit were fabricated by Natsume Optical Co., Koshin Kogagu Co., Keihin Coat Co., Geomatec Co., Technical Co., Nitto Optical Co., and Kogakugiken Co. The development of the structural and thermal systems of the O-unit was supported by MRJ Co. and Orbital Engineering Inc.

Funding The Sunrise III project is funded in Japan by the ISAS/JAXA Small Mission-of-Opportunity program for novel solar observations, JSPS KAKENHI Grant Number 18H05234 and 23K25916 (PI: Y. Katsukawa), and the grant of Joint Research by the National Institutes of Natural Sciences (NINS) (NINS program No. OML032402). The Spanish contribution to Sunrise III SCIP has been supported by the Spanish MCIN/AEI under projects RTI2018-096886-B-C5, and PID2021-125325OB-C5; and from the "Center of Excellence Severo Ochoa" awards to IAA-CSIC (SEV-2017-0709, CEX2021-001131-S), all co-funded by European RE-DEF funds, "A way of making Europe". D.O.S. acknowledges financial support from a *Ramón y Cajal* fellowship. C. Q. N. acknowledges support from the Projects PID2022-136563NB-I00/10.13039/501100011033 and ICTS2022-007828, funded by MICIN and the European Union NextGenerationEU/RTRP. Sunrise III is funded by the Max Planck Foundation, the Strategic Innovations Fund of the President of the Max Planck Society (MPG), the Deutsches Zentrum

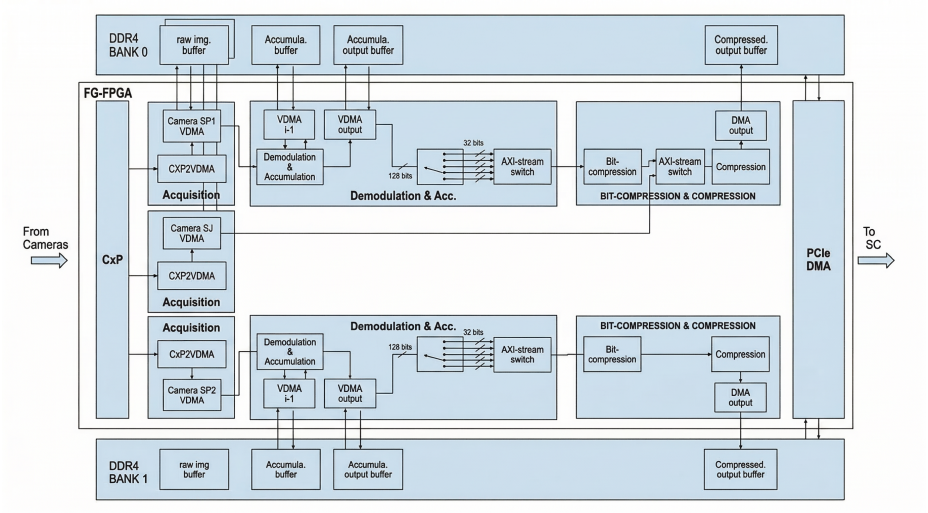


Figure 32. FG processing block diagram.

für Luft und Raumfahrt (DLR), and private donations by supporting members of the Max Planck Society, which is gratefully acknowledged. This project has received funding from the European Research Council (ERC) under the European Union's Horizon 2020 research and innovation programme (grant agreement No. 101097844 — project WINSUN).

Appendix

A. Firmware implementation of SCIP observing modes

Figure 32 shows a simplified block diagram of the image processing blocks inside the architecture of the FG's FPGA (some elements, such as the Double Data Rate (DDR) memory controllers, bus controllers, etc., are not depicted for simplicity). It consists of two almost identical pipelines that process images from the cameras and transfer the reduced scientific data to the SyC through the Peripheral Component Interconnect Express (PCIe) interface.

The pipeline at the bottom of the diagram processes images from the SP2 camera and uses the external DDR bank 1 for buffering intermediate results. The other pipeline, at the top of the image, processes images from the SP1 and SJ cameras and uses the DDR bank 0 in the same way. Since SJ's stream is not demodulated, its acquisition block is directly connected to the compression block of SP1 through an Advanced eXtensible Interface (AXI)-Stream switch.

Several Video Direct Memory Access (VDMA) Intellectual Property cores (IPs) are instantiated in the design. These blocks are provided by Xilinx™ as part of its IP repository and are intended for video frame handling. In the design, each of them is responsible for creating a circular buffer in external memory and performing read/write transfers from/to it with minimum microprocessor intervention. After being configured, a synchronization pulse is enough to trigger a whole image transfer from the buffer to the next processing block. All circular

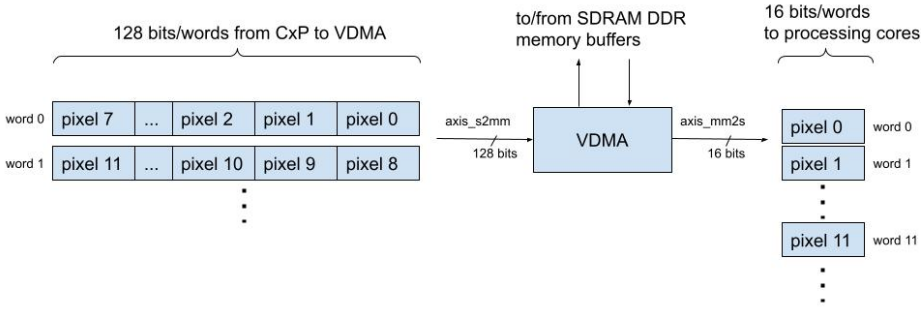


Figure 33. Graphical illustration of the CoaXPress-to-VDMA pixel ordering.

buffers are accessible from the SyC through the PCIe interface, implemented with a Xilinx IP XDMA. During nominal observations, the SyC reads final results from the compression output buffer. However, for testing purposes, it can also read intermediate results from the "raw img." or "Accumula. output" buffers.

All processing blocks are configurable so that they can be enabled, disabled, or bypassed. In such a way, they can accomplish SCIP observation requirements. In the normal mode, all processing blocks are enabled. However, in the rapid mode, the demodulation and accumulation cores as well as the bit-compression core are bypassed. For testing purposes, different configurations can be set to obtain, for example, demodulated images without compression from the Accumula. output buffer.

A.1. Acquisition block

The CoaXPress-to-VDMA block (CxP2VDMA) is the core of the acquisition stage. This block implements a bus translation between the AXI-Stream output bus of the CxP Host core and the AXI-Stream input bus of the VDMA core. This adaptation pursues two main aims: preventing CxP metadata from reaching VDMA, hence avoiding metadata to be mistaken with pixel data, and translating 12 bits-per-pixel (bpp) format to 16 bpp format. The latter is needed since images from the cameras arrive at the FG in 12 bpp format packed into 32-bit words. This pixel-packed format contains a non-integer number of pixels per word (i.e., two pixels + 8 bits of the next pixel), which is undesirable for the rest of the pipeline operations, which are executed in one-pixel per clock cycle flavor. In this context, the CxP2VDMA block unpacks the received pixels, extends its depth to 16 bits and finally pack them into 128-bit words. The Camera VDMA's AXI-Stream ports are asymmetrically configured to match such a bus width and supply the demodulator core with 16 bpp at one pixel per clock cycle as described in Figure 33. For testing purposes, the SyC can read raw images with a pixel de-interleaving format from the raw image buffer.

A.2. Demodulation and accumulation

The demodulation operation carried out during the normal mode consists of multiplying the demodulation matrix by the modulated images pixel by pixel. The demodulation matrix is a 5 × 5 matrix of elements [-1, -0.5, 0, 0.5, 1] whose order (on each row) depends on the PMU rotation phase. As a result, five images corresponding to the four Stokes parameters I_d, Q_d, U_d, V_d, and the pseudo-Stokes parameter R_d are obtained (Kawabata et al. 2022b; Kubo et al. 2023). Such a set of images are accumulated along a configurable number of PMU cycles ranging from $n_{PMU} = 2$ (1.024 s, the shortest integration) to $n_{PMU} = 4$ (2.048 s). The longest integration time of 10.24 s is achieved by acquiring five datasets with $n_{PMU} = 4$ at each slit position. After demodulation and accumulation, the data format changes from unsigned 12 bpp to unsigned 19 bpp for I_d and signed 18 bpp for Q_d, U_d, V_d, and R_d. Note that I_d, Q_d, U_d, V_d, and R_d are results of the demodulation operation and are different from the true Stokes parameters. The true Stokes parameters are retrieved by the polarization calibration described in Section 6.3.

The image demodulation and accumulation block has been designed to perform both operations in a pipeline. In this configuration, demodulation and accumulation are carried out simultaneously (after a small initial latency). The data flow through the core for a demodulation of $N_a = 16\, n_{PMU}$ images consists of the following steps:

1. The first image is received, demodulated, and buffered in the accumulation buffer. The PMU phase of the first image is latched and is incremented with every new image received. The output of the demodulation is buffered in a ping-pong buffer, which allows reading from one frame position and writing the result in another frame position without read/write conflicts. Notice that the result of demodulating one single spatial pixel is a set of five interleaved pixel values (I_d, Q_d, U_d, V_d, and R_d), 24-bit wide each, arranged in words of 128-bit each (this includes five padding bits to complete a power-of-two bit width).
2. The following images, up to N_a, are demodulated and accumulated with the previous demodulated image. To do that, the previous demodulated image is read from the accumulation buffer as soon as a new image is received and demodulated. In such a way, synchronization is ensured, and demodulated images can be accumulated pixel by pixel. The resulting image is buffered in the accumulation buffer, except for the last one which is routed to the demodulation output buffer.
3. The demodulation output buffer stores the final demodulation results of I_d, Q_d, U_d, V_d, and R_d in the pixel-interleaving format described above. These images are de-interleaved in order to supply the bit-compression and compression stages with a single image stream. Such a de-interleaving operation is done by means of a pixel selector and an AXI-Stream switch. For each Stokes parameter (including R), the whole buffer is read, but only the bits containing that parameter are selected and packed into 32-bit words.

Table 8. Bit compression parameters

Compression	a	b	c	Note
(bpp)	(DN)	(DN)	(DN^2)	
No	–	–	–	For TEST and RAPID mode
19U to 16U	1006.027	7987.946	-23987910	For Stokes I_d
18S to 16U	1078.459	7843.082	-23836926	For Stokes Q_d, U_d, V_d, and R_d

A.3. Bit-compression

Demodulated and accumulated images, coded as unsigned 19 bpp (for Stokes I_d) and signed 18 bpp (for Stokes Q_d, U_d, V_d, and R_d) values, are pre-processed before applying the standard image compression algorithm. Such a process, named bit-compression, transforms the unsigned 19 bpp and signed 18 bpp data to unsigned 16 bpp data. To ensure precision in the small value range, a threshold N_c is established, below which no compression is carried out. $N_\mathrm{c} = 5000$ DN by default, but it can be parameterized after laboratory tests. Bit-compression is given by

$$X = \texttt{round}(a + \sqrt{bN + c}), \tag{3}$$

where N stands for the input pixel value ($N > N_\mathrm{c}$) and X stands for the bit-compressed pixel value. Table 8 shows parameters a, b, and c for the different types of compression: no bit-compression, unsigned 19 bpp to unsigned 16 bpp, and signed 18 bpp to unsigned 16 bpp. Signal losses induced by the bit-compression step are more than five times smaller than the expected photon noise and can therefore be considered negligible (Kubo et al. 2023). The bit-compression parameters listed in Table 8 differ from those described in (Kubo et al. 2023) because they were updated to better align with the planned flight operations in 2024.

A custom bit-compression, FPGA core is designed to accomplish the SCIP's data reduction needs. It uses a dedicated fixed-point architecture together with a Coordinate Rotation Digital Computer (CORDIC) Xilinx IP core to calculate the square root. The core is implemented as a hardware block that works in a pipeline manner after an initial latency. That is, it accepts one input value per clock cycle and produces one result per clock cycle. All figures for a, b, and c in Table 8 are significant to provide the required precision, once they are represented as fixed-point values (after multiplication by an integer power of 2), each with a given bit width. Note that, when working in fixed-point precision, the threshold application to the input data can simply be done by bit selection, discarding the fractional part.[2] Additionally, divisions by a power of 2 can be

[2]The threshold application also ensures the radicand in Eq. (3) is positive.

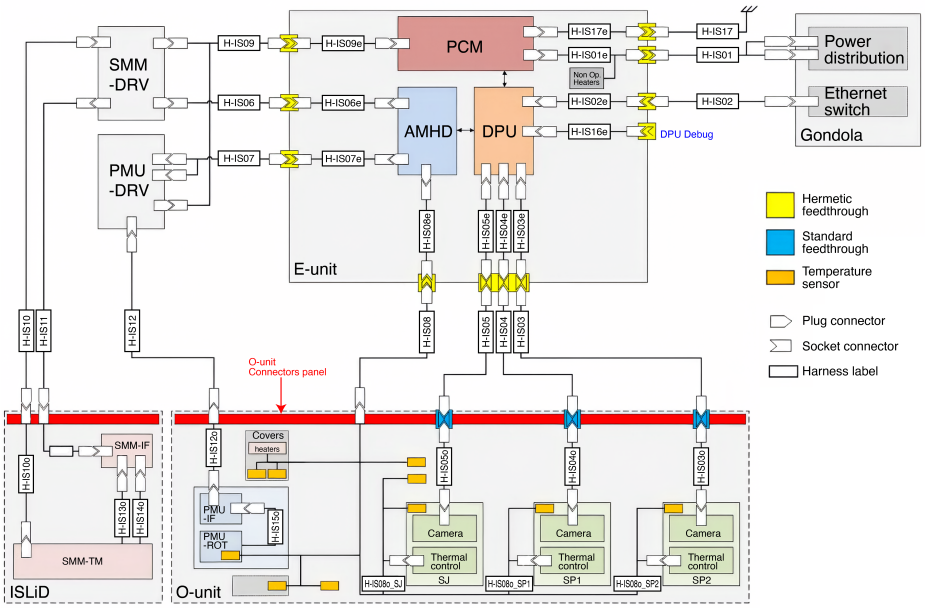


Figure 34. Detailed harness block diagram of SCIP.

implemented through a bit shift or directly discarding the corresponding less-significant bits.

A.4. Compression

The last stage in the processing pipeline is an image compression block. The core of this block is the IP Sunrise Lossless Compression (SLOC) which implements the standard CCSDS-LDC 121.0-B2, a low-complexity solution to compress any kind of data including 2D images. This core performs one pixel per clock cycle at a frequency of 150 MHz to achieve the real-time processing required in SCIP and TuMag instruments (Sánchez et al. 2022). Note that the image compression was not used during the flight in July 2024.

B. SCIP harness

The SCIP harness consists of 13 cable bundles external to the E-unit plus some other bundles which are internal to the various units. A block diagram of the harness can be seen in Figure 34. The external bundles interconnect 1) subsystems in the E-unit with those in the O-unit, in the gondola, and the SMM-DRV and PMU-DRV; 2) the SMM-DRV with the SMM-IF, located in the ISLiD; 3) the PMU-DRV with the PMU-IF, located in the O-unit; and 4) the SCIP ground with the system common ground. They are named H-ISXX, where XX is a consecutive number. Internal bundles to the units have a similar definition and materials to the external ones. They are labeled H-ISXXe/o, where “e” and “o”

refer to the E-unit and O-unit, respectively. D-sub connectors have been used for the external harness and a combination of them and Samtec, high-density connectors for the internal bundles. The external bundles receive power from the gondola power distribution, provide communication between the SCIP E-unit and ICS, and carry the signals needed for global control of the instrument. Three of them (H-IS03, 04, and 05) are CxP cables that provide power, control signals for the three cameras, and image transfer from the cameras to the E-unit.

Several considerations have been taken into account in the SCIP harness design. Special care has been taken with cable widths and selection of materials in order to avoid small voltage drops in the long harnesses connecting the E-unit and O-unit and to minimize the outgassing impact in the quasi-vacuum flight conditions. Differential techniques with twisted pairs and external shielding connected to the structure have been adopted for best common-mode noise rejection and ground loop prevention, in order to minimize electromagnetic interference of SCIP with itself and with the other instruments.

References

Barthol, P., Gandorfer, A., Solanki, S.K., Schüssler, M., Chares, B., Curdt, W., Deutsch, W., Feller, A., Germerott, D., Grauf, B., Heerlein, K., Hirzberger, J., Kolleck, M., Meller, R., Müller, R., Riethmüller, T.L., Tomasch, G., Knölker, M., Lites, B.W., Card, G., Elmore, D., Fox, J., Lecinski, A., Nelson, P., Summers, R., Watt, A., Martínez Pillet, V., Bonet, J.A., Schmidt, W., Berkefeld, T., Title, A.M., Domingo, V., Gasent Blesa, J.L., del Toro Iniesta, J.C., López Jiménez, A., Álvarez-Herrero, A., Sabau-Graziati, L., Widani, C., Haberler, P., Härtel, K., Kampf, D., Levin, T., Pérez Grande, I., Sanz-Andrés, A., Schmidt, E.: 2011, The Sunrise Mission. *Solar Phys.* 268, 1. DOI. ADS.

Berkefeld, T., Schmidt, W., Soltau, D., Bell, A., Doerr, H.P., Feger, B., Friedlein, R., Gerber, K., Heidecke, F., Kentischer, T., v. d. Lühe, O., Sigwarth, M., Wälde, E., Barthol, P., Deutsch, W., Gandorfer, A., Germerott, D., Grauf, B., Meller, R., Álvarez-Herrero, A., Knölker, M., Martínez Pillet, V., Solanki, S.K., Title, A.M.: 2011, The Wave-Front Correction System for the Sunrise Balloon-Borne Solar Observatory. *Solar Phys.* 268, 103. DOI. ADS.

Berkefeld, T., Bell, A., Volkmer, R., Heidecke, F., Preis, T., Sonner, T., Nakai, E., Korpi-Lagg, A., Gandorfer, A., Solanki, S.K., del Toro Iniesta, J.C., Katsukawa, Y., Bernasconi, P., Feller, A., Riethmüller, T.L., Álvarez-Herrero, A., Kubo, M., Martínez Pillet, V., Smitha, H.N., Orozco Suárez, D., Grauf, B., Carpenter, M.: 2026, SUNRISE III: The Wavefront Correction System. *Solar Phys.* 301, 57. DOI. ADS.

Bernasconi, P.N., Rust, D.M., Eaton, H.A., Murphy, G.A.: 2000, Balloon-borne telescope for high-resolution solar imaging and polarimetry. In: Melugin, R.K., Röser, H.-P. (eds.) *Airborne Telescope Systems*, *Society of Photo-Optical Instrumentation Engineers (SPIE) Conference Series* 4014, 214. DOI. ADS.

Bernasconi, P., Carpenter, M., Eaton, H., Schulze, E., Carkhuff, B., Palo, G., Young, D., Raouafi, N., Vourlidas, A., Coker, R., Solanki, S.K., Korpi-Lagg, A., Gandorfer, A., Feller, A., Riethmüller, T.L., Smitha, H.N., Grauf, B., del Toro Iniesta, J.C., Orozco Suárez, D., Katsukawa, Y., Kubo, M., Berkefeld, T., Bell, A., Álvarez-Herrero, A., Martínez Pillet, V.: 2025, The Gondola for the SUNRISE III Balloon-Borne Solar Observatory. *Solar Phys.* 300, 112. DOI. ADS.

Centeno, R.: 2018, On the Weak Field Approximation for Ca 8542 Å. *Astrophys. J.* 866, 89. DOI. ADS.

Danilovic, S., Gandorfer, A., Lagg, A., Schüssler, M., Solanki, S.K., Vögler, A., Katsukawa, Y., Tsuneta, S.: 2008, The intensity contrast of solar granulation: comparing Hinode SP results with MHD simulations. *Astron. Astrophys.* 484, L17. DOI. ADS.

Danilovic, S., Beeck, B., Pietarila, A., Schüssler, M., Solanki, S.K., Martínez Pillet, V., Bonet, J.A., del Toro Iniesta, J.C., Domingo, V., Barthol, P., Berkefeld, T., Gandorfer, A., Knölker,

M., Schmidt, W., Title, A.M.: 2010, Transverse Component of the Magnetic Field in the Solar Photosphere Observed by SUNRISE. *Astrophys. J. Lett.* 723, L149. DOI. ADS.

del Toro Iniesta, J.C., Orozco Suárez, D., Álvarez-Herrero, A., Sanchis Kilders, E., Pérez-Grande, I., Ruiz Cobo, B., Bellot Rubio, L.R., Balaguer Jiménez, M., López Jiménez, A.C., Álvarez García, D., Ramos Más, J.L., Cobos Carrascosa, J.P., Labrousse, P., Moreno Mantas, A.J., Morales-Fernández, J.M., Aparicio del Moral, B., Sánchez Gómez, A., Bailón Martínez, E., Bailén, F.J., Strecker, H., Siu-Tapia, A.L., Santamarina Guerrero, P., Moreno Vacas, A., Atiénzar García, J., Dorantes Monteagudo, A.J., Bustamante, I., Tobaruela, A., Fernández-Medina, A., Núñez Peral, A., Cebollero, M., Garranzo-García, D., García Parejo, P., Gonzalo Melchor, A., Sánchez Rodríguez, A., Campos-Jara, A., Laguna, H., Silva-López, M., Blanco Rodríguez, J., Gasent Blesa, J.L., Rodríguez Martínez, P., Ferreres, A., Gilabert Palmer, D., Torralbo, I., Piqueras, J., González-Bárcena, D., Fernández, A.J., Hernández Expósito, D., Páez Mañá, E., Magdaleno Castelló, E., Rodríguez Valido, M., Korpi-Lagg, A., Gandorfer, A., Solanki, S.K., Berkefeld, T., Bernasconi, P., Feller, A., Katsukawa, Y., Riethmüller, T.L., Smitha, H.N., Kubo, M., Martínez Pillet, V., Grauf, B., Bell, A., Carpenter, M.: 2025, TuMag: The Tunable Magnetograph for the SUNRISE III Mission. *Solar Phys.* 300, 148. DOI. ADS.

Elmore, D.: 1990, A Polarization Calibration Technique for the Advanced Stokes Polarimeter, NCAR Technical Notes. DOI. ADS.

Feller, A., Gandorfer, A., Grauf, B., Hölken, J., Iglesias, F.A., Korpi-Lagg, A., Riethmüller, T.L., Staub, J., Fernandez-Rico, G., Castellanos Durán, J.S., Solanki, S.K., Smitha, H.N., Sant, K., Barthol, P., Bayon Laguna, M., Bergmann, M., Bischoff, J., Bochmann, J., Bruns, S., Deutsch, W., Eberhardt, M., Enge, R., Goodyear, S., Heerlein, K., Heinrichs, J., Hirche, D., Meining, S., Mende, R., Meyer, S., Mühlhaus, M., Müller, M.F., Monecke, M., Oberdorfer, D., Papagiannaki, I., Ramanath, S., Vergöhl, M., Vukadinović, D., Werner, S., Zerr, A., Berkefeld, T., Bernasconi, P., Katsukawa, Y., del Toro Iniesta, J.C., Bell, A., Carpenter, M., Álvarez Herrero, A., Kubo, M., Martínez Pillet, V., Orozco Suárez, D.: 2025, The Sunrise Ultraviolet Spectropolarimeter and Imager: Instrument Description. *Solar Phys.* 300, 65. DOI. ADS.

Fernández-Soler, A., Gonzállez, D., Pérez-Grande, I., Sanz-Andrés, A.: 2021, Thermal analysis of SUNRISE III ascent phase. In: *50th International Conference on Environmental Systems*.

Gandorfer, A., Grauf, B., Barthol, P., Riethmüller, T.L., Solanki, S.K., Chares, B., Deutsch, W., Ebert, S., Feller, A., Germerott, D., Heerlein, K., Heinrichs, J., Hirche, D., Hirzberger, J., Kolleck, M., Meller, R., Müller, R., Schäfer, R., Tomasch, G., Knölker, M., Martínez Pillet, V., Bonet, J.A., Schmidt, W., Berkefeld, T., Feger, B., Heidecke, F., Soltau, D., Tischenberg, A., Fischer, A., Title, A., Anwand, H., Schmidt, E.: 2011, The Filter Imager SuFI and the Image Stabilization and Light Distribution System ISLiD of the Sunrise Balloon-Borne Observatory: Instrument Description. *Solar Phys.* 268, 35. DOI. ADS.

González-Bárcena, D., Pérez-Grande, I., Sanz-Andrés, Á., González-Llana, A.: 2017, Methodology for the thermal analysis of instrumentation in Long Duration Balloon missions. In: *European conference for aeronautics and space sciences (EUCASS)*.

González-Llana, A., González-Bárcena, D., Pérez-Grande, I., Sanz-Andrés, Á.: 2018, Selection of extreme environmental conditions, albedo coefficient and Earth infrared radiation, for polar summer Long Duration Balloon missions. *Acta Astronautica* 148, 276. DOI. ADS.

Ichimoto, K., Lites, B., Elmore, D., Suematsu, Y., Tsuneta, S., Katsukawa, Y., Shimizu, T., Shine, R., Tarbell, T., Title, A., Kiyohara, J., Shinoda, K., Card, G., Lecinski, A., Streander, K., Nakagiri, M., Miyashita, M., Noguchi, M., Hoffmann, C., Cruz, T.: 2008, Polarization Calibration of the Solar Optical Telescope onboard Hinode. *Solar Phys.* 249, 233. DOI. ADS.

Ishikawa, S., Shimizu, T., Kano, R., Bando, T., Ishikawa, R., Giono, G., Tsuneta, S., Nakayama, S., Tajima, T.: 2015, Development of a Precise Polarization Modulator for UV Spectropolarimetry. *Solar Phys.* 290, 3081. DOI. ADS.

Jafarzadeh, S., Solanki, S.K., Gafeira, R., van Noort, M., Barthol, P., Blanco Rodríguez, J., del Toro Iniesta, J.C., Gandorfer, A., Gizon, L., Hirzberger, J., Knölker, M., Orozco Suárez, D., Riethmüller, T.L., Schmidt, W.: 2017, Transverse Oscillations in Slender Ca II H Fibrils Observed with Sunrise/SuFI. *Astrophys. J. Supp. Series* 229, 9. DOI. ADS.

Katsukawa, Y.: 2018, Penumbral Microjets in Sunspot Chromospheres: Evidence of Magnetic Reconnection. In: Shimizu, T., Imada, S., Kubo, M. (eds.) *First Ten Years of Hinode Solar On-Orbit Observatory*, *Astrophysics and Space Science Library* 449, 201. DOI. ADS.

Katsukawa, Y., del Toro Iniesta, J.C., Solanki, S.K., Kubo, M., Hara, H., Shimizu, T., Oba, T., Kawabata, Y., Tsuzuki, T., Uraguchi, F., Nodomi, Y., Shinoda, K., Tamura, T., Suematsu,

Y., Ishikawa, R., Kano, R., Matsumoto, T., Ichimoto, K., Nagata, S., Quintero Noda, C., Anan, T., Orozco Suárez, D., Balaguer Jiménez, M., López Jiménez, A.C., Cobos Carrascosa, J.P., Feller, A., Riethmueller, T., Gandorfer, A., Lagg, A.: 2020, Sunrise Chromospheric Infrared SpectroPolarimeter (SCIP) for sunrise III: system design and capability. In: Evans, C.J., Bryant, J.J., Motohara, K. (eds.) *Ground-based and Airborne Instrumentation for Astronomy VIII*, *Society of Photo-Optical Instrumentation Engineers (SPIE) Conference Series* 11447, 114470Y. DOI. ADS.

Katsukawa, Y., Hara, H., Kubo, M., Kawabata, Y., Oba, T., Piqueras Carreño, J., Pérez Grande, I., Shinoda, K., Tamura, T., Uraguchi, F., Tsuzuki, T., Nodomi, Y., Shimizu, T., López Jiménez, A.C., Balaguer Jiménez, M., Álvarez García, D.: 2022, Sunrise chromospheric Infrared spectroPolarimeter (SCIP) for SUNRISE III: thermal-vacuum test of the SCIP optical unit. In: Evans, C.J., Bryant, J.J., Motohara, K. (eds.) *Ground-based and Airborne Instrumentation for Astronomy IX*, *Society of Photo-Optical Instrumentation Engineers (SPIE) Conference Series* 12184, 121842B. DOI. ADS.

Kawabata, Y., Katsukawa, Y., Tsuzuki, T., Uraguchi, F., Mitsui, K., Shinoda, K., Tamura, T., Nodomi, Y., Hara, H., Kubo, M.: 2022a, Optical alignment and performance evaluation of the Sunrise Chromospheric Infrared spectroPolarimeter (SCIP) for SUNRISE III. In: Evans, C.J., Bryant, J.J., Motohara, K. (eds.) *Ground-based and Airborne Instrumentation for Astronomy IX*, *Society of Photo-Optical Instrumentation Engineers (SPIE) Conference Series* 12184, 1218427. DOI. ADS.

Kawabata, Y., Katsukawa, Y., Kubo, M., Anan, T., Ichimoto, K., Shinoda, K., Tsuzuki, T., Uraguchi, F., Nagata, S., Oba, T., Expósito, D.H., Sánchez Gómez, A., Orozco Suárez, D., Balaguer Jiménz, M., Bailón Martínez, E., Morales Fernández, J.M., Moreno Mantas, A., del Toro Iniesta, J.C., Gandorfer, A., Feller, A.: 2022b, Polarimetric calibration of a spectropolarimeter instrument with high precision: Sunrise chromospheric infrared spectropolarimeter (SCIP) for the sunrise iii balloon telescope. *Appl. Opt.* 61, 9716. DOI. ADS.

Kawabata, Y., Quintero Noda, C., Katsukawa, Y., Kubo, M., Matsumoto, T., Oba, T.: 2024, Multiline Stokes Synthesis of Ellerman Bombs: Obtaining Seamless Information from Photosphere to Chromosphere. *Astrophys. J.* 960, 26. DOI. ADS.

Korpi-Lagg, A., Gandorfer, A., Solanki, S.K., del Toro Iniesta, J.C., Katsukawa, Y., Bernasconi, P., Berkefeld, T., Feller, A., Riethmüller, T.L., Álvarez-Herrero, A., Kubo, M., Martínez Pillet, V., Smitha, H.N., Orozco Suárez, D., Grauf, B., Carpenter, M., Bell, A., Álvarez-Alonso, M.-T., Álvarez García, D., Aparicio del Moral, B., Atiénzar, J., Ayoub, D., Bailén, F.J., Bailón Martínez, E., Balaguer Jiménez, M., Barthol, P., Bayon Laguna, M., Bellot Rubio, L.R., Bergmann, M., Blanco Rodríguez, J., Bochmann, J., Borrero, J.M., Campos-Jara, A., Castellanos Durán, J.S., Cebollero, M., Conde Rodríguez, A., Deutsch, W., Eaton, H., Fernández-Medina, A.B., Fernandez-Rico, G., Ferreres, A., García, A., García Alarcia, R.M., García Parejo, P., Garranzo-García, D., Gasent Blesa, J.L., Gerber, K., Germerott, D., Gilabert Palmer, D., Gizon, L., Gómez Sánchez-Tirado, M.A., González-Bárcena, D., Gonzalo Melchor, A., Goodyear, S., Hara, H., Harnes, E., Heerlein, K., Heidecke, F., Heinrichs, J., Hernández Expósito, D., Hirzberger, J., Hoelken, J., Hyun, S., Iglesias, F.A., Ishikawa, R.T., Jeon, M., Kawabata, Y., Kolleck, M., Laguna, H., Lomas, J., López Jiménez, A.C., Manzano, P., Matsumoto, T., Mayo Turrado, D., Meierdierks, T., Meining, S., Monecke, M., Morales-Fernández, J.M., Moreno Mantas, A.J., Moreno Vacas, A., Müller, M.F., Müller, R., Naito, Y., Nakai, E., Núñez Peral, A., Oba, T., Palo, G., Pérez-Grande, I., Piqueras Carreño, J., Preis, T., Przybylski, D., Quintero Noda, C., Ramanath, S., Ramos Más, J.L., Raouafi, N., Rivas-Martínez, M.-J., Rodríguez Martínez, P., Rodríguez Valido, M., Ruiz Cobo, B., Sánchez Rodríguez, A., Sanchez Toledo, M., Sánchez Gómez, A., Sanchis Kilders, E., Sant, K., Santamarina Guerrero, P., Schulze, E., Shimizu, T., Silva-López, M., Singh, K., Siu-Tapia, A.L., Sonner, T., Staub, J., Strecker, H., Tobaruela, A., Torralbo, I., Tritschler, A., Tsuzuki, T., Uraguchi, F., Volkmer, R., Vourlidas, A., Vukadinović, D., Werner, S., Zerr, A.: 2025, SUNRISE III: Overview of Observatory and Instruments. *Solar Phys.* 300, 75. DOI. ADS.

Kubo, M., Shimizu, T., Katsukawa, Y., Kawabata, Y., Anan, T., Ichimoto, K., Shinoda, K., Tamura, T., Nodomi, Y., Nakayama, S., Yamada, T., Tajima, T., Nakata, S., Nakajima, Y., Okutani, K., Feller, A., del Toro Iniesta, J.C.: 2020, Sunrise Chromospheric Infrared spectroPolarimeter (SCIP) for SUNRISE III: polarization modulation unit. In: Evans, C.J., Bryant, J.J., Motohara, K. (eds.) *Ground-based and Airborne Instrumentation for Astronomy VIII*, *Society of Photo-Optical Instrumentation Engineers (SPIE) Conference Series* 11447, 11447A3. DOI. ADS.

Kubo, M., Shimizu, T., Katsukawa, Y., Kawabata, Y., Shinoda, K., Anan, T., Ichimoto, K., Tamura, T., Nodomi, Y., Nakayama, S., Yamada, T., Tajima, T., Nakata, S., Nakajima, Y., Okutani, K., Solanki, S.K., del Toro Iniesta, J.C.: 2021, Development of the Polarization Modulation Unit for SUNRISE-3/SCIP. *JAXA Research and Development Report* JAXA-RR-20-009, 83. DOI.

Kubo, M., Katsukawa, Y., Hernández Expósito, D., Sánchez Gómez, A., Balaguer Jimenéz, M., Orozco Suárez, D., Morales Fernández, J.M., Aparicio del Moral, B., Moreno Mantas, A.J., Bailón Martínez, E., del Toro Iniesta, J.C., Kawabata, Y., Quintero Noda, C., Oba, T., Ishikawa, R.T., Shimizu, T.: 2023, High-speed data processing onboard sunrise chromospheric infrared spectropolarimeter for the SUNRISE III balloon telescope. *Journal of Astronomical Telescopes, Instruments, and Systems* 9, 034003. DOI. ADS.

Kurucz, R.L., Furenlid, I., Brault, J., Testerman, L.: 1984, *Solar flux atlas from 296 to 1300 nm*. ADS.

Lagg, A., Solanki, S.K., Riethmüller, T.L., Martínez Pillet, V., Schüssler, M., Hirzberger, J., Feller, A., Borrero, J.M., Schmidt, W., del Toro Iniesta, J.C., Bonet, J.A., Barthol, P., Berkefeld, T., Domingo, V., Gandorfer, A., Knölker, M., Title, A.M.: 2010, Fully Resolved Quiet-Sun Magnetic flux Tube Observed with the SUNRISE/IMAX Instrument. *Astrophys. J. Lett.* 723, L164. DOI. ADS.

Lagg, A., Lites, B., Harvey, J., Gosain, S., Centeno, R.: 2017, Measurements of Photospheric and Chromospheric Magnetic Fields. *Space Sci. Rev.* 210, 37. DOI. ADS.

Lites, B.W., Akin, D.L., Card, G., Cruz, T., Duncan, D.W., Edwards, C.G., Elmore, D.F., Hoffmann, C., Katsukawa, Y., Katz, N., Kubo, M., Ichimoto, K., Shimizu, T., Shine, R.A., Streander, K.V., Suematsu, A., Tarbell, T.D., Title, A.M., Tsuneta, S.: 2013, The Hinode Spectro-Polarimeter. *Solar Phys.* 283, 579. DOI. ADS.

Martínez Pillet, V., del Toro Iniesta, J.C., Álvarez-Herrero, A., Domingo, V., Bonet, J.A., González Fernández, L., López Jiménez, A., Pastor, C., Gasent Blesa, J.L., Mellado, P., Piqueras, J., Aparicio, B., Balaguer, M., Ballesteros, E., Belenguer, T., Bellot Rubio, L.R., Berkefeld, T., Collados, M., Deutsch, W., Feller, A., Girela, F., Grauf, B., Heredero, R.L., Herranz, M., Jerónimo, J.M., Laguna, H., Meller, R., Menéndez, M., Morales, R., Orozco Suárez, D., Ramos, G., Reina, M., Ramos, J.L., Rodríguez, P., Sánchez, A., Uribe-Patarroyo, N., Barthol, P., Gandorfer, A., Knoelker, M., Schmidt, W., Solanki, S.K., Vargas Domínguez, S.: 2011, The Imaging Magnetograph eXperiment (IMaX) for the Sunrise Balloon-Borne Solar Observatory. *Solar Phys.* 268, 57. DOI. ADS.

Matsumoto, T., Kawabata, Y., Katsukawa, Y., Iijima, H., Quintero Noda, C.: 2023, Synthesis of infrared Stokes spectra in an evolving solar chromospheric jet. *Mon. Not. Roy. Astron. Soc.* 523, 974. DOI. ADS.

Oba, T., Shimizu, T., Katsukawa, Y., Kubo, M., Uraguchi, F., Tsuzuki, T., Tamura, T., Shinoda, K., Kodeki, K., Fukushima, K., Gandorfer, A., del Toro Iniesta, J.C.: 2020, SUNRISE Chromospheric Infrared spectroPolarimeter (SCIP) for SUNRISE III: Scan mirror mechanism. In: Marshall, H.K., Spyromilio, J., Usuda, T. (eds.) *Ground-based and Airborne Telescopes VIII*, *Society of Photo-Optical Instrumentation Engineers (SPIE) Conference Series* 11445, 114454F. DOI. ADS.

Oba, T., Shimizu, T., Katsukawa, Y., Kubo, M., Kawabata, Y., Hara, H., Uraguchi, F., Tsuzuki, T., Tamura, T., Shinoda, K., Kodeki, K., Fukushima, K., Morales Fernández, J.M., Sánchez Gómez, A., Balaguer Jimenéz, M., Hernández Expósito, D., Gandorfer, A.: 2022, Development of Fast and Precise Scan Mirror Mechanism for an Airborne Solar Telescope. *Solar Phys.* 297, 114. DOI. ADS.

Orozco Suárez, D., Álvarez García, D., López Jiménez, A.C., Balaguer Jiménez, M., Hernández Expósito, D., Labrousse, P., Bailén, F.J., Bustamante Díaz, I., Bailón Martínez, E., Aparicio del Moral, B., Morales Fernández, J.M., Sánchez Gómez, A., Tobaruela Abarca, Á., Moreno Mantas, A.J., Ramos Más, J.L., Pérez Grande, I., Piqueras Carreño, J., Katsukawa, Y., Kubo, M., Kawabata, Y., Oba, T., Rodríguez Valido, M., Magdaleno Castelló, E., Del Toro Iniesta, J.C.: 2023, SPGCam: A specifically tailored camera for solar observations. *Frontiers in Astronomy and Space Sciences* 10, 1167540. DOI. ADS.

Piqueras, J., Katsukawa, Y., Gonzalez-Barcena, D., Fernandez-Soler, A., Torralbo, I., Hara, H., Kubo, M., Tamura, T.: 2025, Thermal design and modeling of the SCIP instrument for the Sunrise III mission. *JAXA Research and Development Report* JAXA-RR-24-005, 99. DOI.

Quintero Noda, C., Shimizu, T., Katsukawa, Y., de la Cruz Rodríguez, J., Carlsson, M., Anan, T., Oba, T., Ichimoto, K., Suematsu, Y.: 2017a, Chromospheric polarimetry through

multiline observations of the 850-nm spectral region. *Mon. Not. Roy. Astron. Soc.* 464, 4534. DOI. ADS.

Quintero Noda, C., Kato, Y., Katsukawa, Y., Oba, T., de la Cruz Rodríguez, J., Carlsson, M., Shimizu, T., Orozco Suárez, D., Ruiz Cobo, B., Kubo, M., Anan, T., Ichimoto, K., Suematsu, Y.: 2017b, Chromospheric polarimetry through multiline observations of the 850-nm spectral region - II. A magnetic flux tube scenario. *Mon. Not. Roy. Astron. Soc.* 472, 727. DOI. ADS.

Quintero Noda, C., Uitenbroek, H., Katsukawa, Y., Shimizu, T., Oba, T., Carlsson, M., Orozco Suárez, D., Ruiz Cobo, B., Kubo, M., Anan, T., Ichimoto, K., Suematsu, Y.: 2017c, Solar polarimetry through the K I lines at 770 nm. *Mon. Not. Roy. Astron. Soc.* 470, 1453. DOI. ADS.

Quintero Noda, C., Villanueva, G.L., Katsukawa, Y., Solanki, S.K., Orozco Suárez, D., Ruiz Cobo, B., Shimizu, T., Oba, T., Kubo, M., Anan, T., Ichimoto, K., Suematsu, Y.: 2018a, Solar polarimetry in the K I D_2 line : A novel possibility for a stratospheric balloon. *Astron. Astrophys.* 610, A79. DOI. ADS.

Quintero Noda, C., Uitenbroek, H., Carlsson, M., Orozco Suárez, D., Katsukawa, Y., Shimizu, T., Ruiz Cobo, B., Kubo, M., Oba, T., Kawabata, Y., Hasegawa, T., Ichimoto, K., Anan, T., Suematsu, Y.: 2018b, Study of the polarization produced by the Zeeman effect in the solar Mg I b lines. *Mon. Not. Roy. Astron. Soc.* 481, 5675. DOI. ADS.

Quintero Noda, C., Iijima, H., Katsukawa, Y., Shimizu, T., Carlsson, M., de la Cruz Rodríguez, J., Ruiz Cobo, B., Orozco Suárez, D., Oba, T., Anan, T., Kubo, M., Kawabata, Y., Ichimoto, K., Suematsu, Y.: 2019, Chromospheric polarimetry through multiline observations of the 850 nm spectral region III: Chromospheric jets driven by twisted magnetic fields. *Mon. Not. Roy. Astron. Soc.* 486, 4203. DOI. ADS.

Rast, M.P., Bello González, N., Bellot Rubio, L., Cao, W., Cauzzi, G., Deluca, E., de Pontieu, B., Fletcher, L., Gibson, S.E., Judge, P.G., Katsukawa, Y., Kazachenko, M.D., Khomenko, E., Landi, E., Martínez Pillet, V., Petrie, G.J.D., Qiu, J., Rachmeler, L.A., Rempel, M., Schmidt, W., Scullion, E., Sun, X., Welsch, B.T., Andretta, V., Antolin, P., Ayres, T.R., Balasubramaniam, K.S., Ballai, I., Berger, T.E., Bradshaw, S.J., Campbell, R.J., Carlsson, M., Casini, R., Centeno, R., Cranmer, S.R., Criscuoli, S., Deforest, C., Deng, Y., Erdélyi, R., Fedun, V., Fischer, C.E., González Manrique, S.J., Hahn, M., Harra, L., Henriques, V.M.J., Hurlburt, N.E., Jaeggli, S., Jafarzadeh, S., Jain, R., Jefferies, S.M., Keys, P.H., Kowalski, A.F., Kuckein, C., Kuhn, J.R., Kuridze, D., Liu, J., Liu, W., Longcope, D., Mathioudakis, M., McAteer, R.T.J., McIntosh, S.W., McKenzie, D.E., Miralles, M.P., Morton, R.J., Muglach, K., Nelson, C.J., Panesar, N.K., Parenti, S., Parnell, C.E., Poduval, B., Reardon, K.P., Reep, J.W., Schad, T.A., Schmit, D., Sharma, R., Socas-Navarro, H., Srivastava, A.K., Sterling, A.C., Suematsu, Y., Tarr, L.A., Tiwari, S., Tritschler, A., Verth, G., Vourlidas, A., Wang, H., Wang, Y.-M., NSO and DKIST Project, DKIST Instrument Scientists, DKIST Science Working Group, DKIST Critical Science Plan Community: 2021, Critical Science Plan for the Daniel K. Inouye Solar Telescope (DKIST). *Solar Phys.* 296, 70. DOI. ADS.

Riethmüller, T.L., Solanki, S.K., Hirzberger, J., Danilovic, S., Barthol, P., Berkefeld, T., Gandorfer, A., Gizon, L., Knölker, M., Schmidt, W., Del Toro Iniesta, J.C.: 2013, First High-resolution Images of the Sun in the 2796 Å Mg II k Line. *Astrophys. J. Lett.* 776, L13. DOI. ADS.

Sánchez, A., Barrios, Y., Sarmiento, R., Expósito, D.H., Gómez, A.S.: 2022, A lossless compression solution for SCIP and TuMag instruments aboard of SUNRISE III balloon-borne Solar Observatory. In: *2022 37th Conference on Design of Circuits and Integrated Circuits (DCIS)*, 01.

Scherrer, P.H., Bogart, R.S., Bush, R.I., Hoeksema, J.T., Kosovichev, A.G., Schou, J., Rosenberg, W., Springer, L., Tarbell, T.D., Title, A., Wolfson, C.J., Zayer, I., MDI Engineering Team: 1995, The Solar Oscillations Investigation - Michelson Doppler Imager. *Solar Phys.* 162, 129. DOI. ADS.

Scherrer, P.H., Schou, J., Bush, R.I., Kosovichev, A.G., Bogart, R.S., Hoeksema, J.T., Liu, Y., Duvall, T.L., Zhao, J., Title, A.M., Schrijver, C.J., Tarbell, T.D., Tomczyk, S.: 2012, The Helioseismic and Magnetic Imager (HMI) Investigation for the Solar Dynamics Observatory (SDO). *Solar Phys.* 275, 207. DOI. ADS.

Shimizu, T., Watanabe, K., Nakayama, S., Tajima, T., Obara, S., Imada, S., Nishizuka, N., Ishikawa, S.-n., Hara, H.: 2014, New developments in rotating and linear motion mechanisms used in contamination sensitive space telescopes. In: Navarro, R., Cunningham, C.R., Barto, A.A. (eds.) *Advances in Optical and Mechanical Technologies for Telescopes and*

Instrumentation, *Society of Photo-Optical Instrumentation Engineers (SPIE) Conference Series* 9151, 915138. DOI. ADS.

Shimizu, T., Watanabe, K., Kawabata, Y., Oba, T., Iida, Y., Lee, K., Kano, R., Ishikawa, S., Doi, T., Hasegawa, T., Quintero Noda, C.: 2018, Rotating Mechanism for Space Telescopes: Long Lifetime Performance in Vacuum Environment. *JAXA Research and Development Report* JAXA-RR-18-003, 1. DOI.

Smith, W.J.: 2007, *Modern Optical Engineering: The Design of Optical Systems*, 4th edn. McGraw-Hill, New York. ISBN 9780071476874.

Solanki, S.K., Barthol, P., Danilovic, S., Feller, A., Gandorfer, A., Hirzberger, J., Riethmüller, T.L., Schüssler, M., Bonet, J.A., Martínez Pillet, V., del Toro Iniesta, J.C., Domingo, V., Palacios, J., Knölker, M., Bello González, N., Berkefeld, T., Franz, M., Schmidt, W., Title, A.M.: 2010, SUNRISE: Instrument, Mission, Data, and First Results. *Astrophys. J. Lett.* 723, L127. DOI. ADS.

Solanki, S.K., del Toro Iniesta, J.C., Woch, J., Gandorfer, A., Hirzberger, J., Alvarez-Herrero, A., Appourchaux, T., Martínez Pillet, V., Pérez-Grande, I., Sanchis Kilders, E., Schmidt, W., Gómez Cama, J.M., Michalik, H., Deutsch, W., Fernandez-Rico, G., Grauf, B., Gizon, L., Heerlein, K., Kolleck, M., Lagg, A., Meller, R., Müller, R., Schühle, U., Staub, J., Albert, K., Alvarez Copano, M., Beckmann, U., Bischoff, J., Busse, D., Enge, R., Frahm, S., Germerott, D., Guerrero, L., Löptien, B., Meierdierks, T., Oberdorfer, D., Papagiannaki, I., Ramanath, S., Schou, J., Werner, S., Yang, D., Zerr, A., Bergmann, M., Bochmann, J., Heinrichs, J., Meyer, S., Monecke, M., Müller, M.-F., Sperling, M., Álvarez García, D., Aparicio, B., Balaguer Jiménez, M., Bellot Rubio, L.R., Cobos Carracosa, J.P., Girela, F., Hernández Expósito, D., Herranz, M., Labrousse, P., López Jiménez, A., Orozco Suárez, D., Ramos, J.L., Barandiarán, J., Bastide, L., Campuzano, C., Cebollero, M., Dávila, B., Fernández-Medina, A., García Parejo, P., Garranzo-García, D., Laguna, H., Martín, J.A., Navarro, R., Núñez Peral, A., Royo, M., Sánchez, A., Silva-López, M., Vera, I., Villanueva, J., Fourmond, J.-J., de Galarreta, C.R., Bouzit, M., Hervier, V., Le Clec'h, J.C., Szwec, N., Chaigneau, M., Buttice, V., Dominguez-Tagle, C., Philippon, A., Boumier, P., Le Cocguen, R., Baranjuk, G., Bell, A., Berkefeld, T., Baumgartner, J., Heidecke, F., Maue, T., Nakai, E., Scheiffelen, T., Sigwarth, M., Soltau, D., Volkmer, R., Blanco Rodríguez, J., Domingo, V., Ferreres Sabater, A., Gasent Blesa, J.L., Rodríguez Martínez, P., Osorno Caudel, D., Bosch, J., Casas, A., Carmona, M., Herms, A., Roma, D., Alonso, G., Gómez-Sanjuan, A., Piqueras, J., Torralbo, I., Fiethe, B., Guan, Y., Lange, T., Michel, H., Bonet, J.A., Fahmy, S., Müller, D., Zouganelis, I.: 2020, The Polarimetric and Helioseismic Imager on Solar Orbiter. *Astron. Astrophys.* 642, A11. DOI. ADS.

Trujillo Bueno, J., del Pino Alemán, T.: 2022, Magnetic Field Diagnostics in the Solar Upper Atmosphere. *Annu. Rev. Astron. Astrophys.* 60, 415. DOI. ADS.

Tsuneta, S., Ichimoto, K., Katsukawa, Y., Nagata, S., Otsubo, M., Shimizu, T., Suematsu, Y., Nakagiri, M., Noguchi, M., Tarbell, T., Title, A., Shine, R., Rosenberg, W., Hoffmann, C., Jurcevich, B., Kushner, G., Levay, M., Lites, B., Elmore, D., Matsushita, T., Kawaguchi, N., Saito, H., Mikami, I., Hill, L.D., Owens, J.K.: 2008, The Solar Optical Telescope for the Hinode Mission: An Overview. *Solar Phys.* 249, 167. DOI. ADS.

Tsuzuki, T., Katsukawa, Y., Uraguchi, F., Hara, H., Kubo, M., Nodomi, Y., Suematsu, Y., Kawabata, Y., Shimizu, T., Gandorfer, A., Feller, A., Grauf, B., Solanki, S., Carlos del Toro Iniesta, J.: 2020, Sunrise Chromospheric Infrared spectroPolarimeter (SCIP) for SUNRISE III: optical design and performance. In: Evans, C.J., Bryant, J.J., Motohara, K. (eds.) *Ground-based and Airborne Instrumentation for Astronomy VIII*, *Society of Photo-Optical Instrumentation Engineers (SPIE) Conference Series* 11447, 11447AJ. DOI. ADS.

Uraguchi, F., Tsuzuki, T., Katsukawa, Y., Hara, H., Iwamura, S., Kubo, M., Nodomi, Y., Suematsu, Y., Kawabata, Y., Shimizu, T., Gandorfer, A., del Toro Iniesta, J.C.: 2020, Sunrise Chromospheric Infrared spectroPolarimeter (SCIP) for SUNRISE III: opto-mechanical analysis and design. In: Evans, C.J., Bryant, J.J., Motohara, K. (eds.) *Ground-based and Airborne Instrumentation for Astronomy VIII*, *Society of Photo-Optical Instrumentation Engineers (SPIE) Conference Series* 11447, 11447AB. DOI. ADS.

Uraguchi, F., Katsukawa, Y., Hara, H., Shimizu, T., Tsuzuki, T., Nodomi, Y., Kubo, M., Kawabata, Y., Oba, T., Iwamura, S.: 2023, Opto-mechanical analysis of Sunrise Chromospheric Infrared spectroPolarimeter (SCIP) for SUNRISE III Balloon Telescope. *JAXA Research and Development Report* JAXA-RR-22-008, 51. DOI.

Wedemeyer-Böhm, S., Lagg, A., Nordlund, Å.: 2009, Coupling from the Photosphere to the Chromosphere and the Corona. *Space Sci. Rev.* 144, 317. DOI. ADS.